JADES: primaeval Lyman α emitting galaxies reveal early sites of reionization out to redshift $z \sim 9$

Joris Witstok [1,2,3,4]★ Roberto Maiolino [1,2,5]★ Renske Smit [6] Gareth C. Jones [7]
Andrew J. Bunker [7] Jakob M. Helton [8] Benjamin D. Johnson [9] Sandro Tacchella [1,2]
Aayush Saxena [5,7] Santiago Arribas [10] Rachana Bhatawdekar [11] Kristan Boyett [12,13]
Alex J. Cameron [7] Phillip A. Cargile [9] Stefano Carniani [14] Stéphane Charlot [15]
Jacopo Chevallard [7] Mirko Curti [16] Emma Curtis-Lake [17] Francesco D'Eugenio [1,2]
Daniel J. Eisenstein [9] Kevin Hainline [8] Ryan Hausen [18] Nimisha Kumari [19] Isaac Laseter [20]
Michael V. Maseda [20] Marcia Rieke [8] Brant Robertson [21] Jan Scholtz [1,2] Irene Shivaei [10]
Christina C. Williams [22] Christopher N. A. Willmer [8] and Chris Willott [23]

Affiliations are listed at the end of the paper

ABSTRACT

Given the sensitivity of the resonant Lyman α (Ly α) transition to absorption by neutral hydrogen, observations of Ly α emitting galaxies (LAEs) have been widely used to probe the ionizing capabilities of reionization-era galaxies and their impact on the intergalactic medium (IGM). However, prior to *JWST* our understanding of the contribution of fainter sources and of ionized 'bubbles' at earlier stages of reionization remained uncertain. Here, we present the characterization of three exceptionally distant LAEs at $z > 8$, newly discovered by *JWST*/Near-Infrared Spectrograph in the JADES survey. These three similarly bright ($M_{\mathrm{UV}} \approx -20\,\mathrm{mag}$) LAEs exhibit small Ly α velocity offsets from the systemic redshift, $\Delta v_{\mathrm{Ly}\alpha} \lesssim 200\,\mathrm{km\,s}^{-1}$, yet span a range of Ly α equivalent widths (15, 31, and 132 Å). The former two show moderate Ly α escape fractions ($f_{\mathrm{esc,\,Ly}\alpha} \approx 10\,\mathrm{per\,cent}$), whereas Ly α escapes remarkably efficiently from the third ($f_{\mathrm{esc,\,Ly}\alpha} \approx 72\,\mathrm{per\,cent}$), which moreover is very compact (half-light radius of $90 \pm 10\,\mathrm{pc}$). We find these LAEs are low-mass galaxies dominated by very recent, vigorous bursts of star formation accompanied by strong nebular emission from metal-poor gas. We infer the two LAEs with modest $f_{\mathrm{esc,\,Ly}\alpha}$, one of which reveals evidence for ionization by an active galactic nucleus, may have reasonably produced small ionized bubbles preventing complete IGM absorption of Ly α. The third, however, requires a ~ 3 physical Mpc bubble, indicating faint galaxies have contributed significantly. The most distant LAEs thus continue to be powerful observational probes into the earlier stages of reionization.

Key words: methods: observational – techniques: spectroscopic – galaxies: high-redshift – dark ages, reionization, first stars.

1 INTRODUCTION

Cosmic reionization is the crucial phase transition initiated by the formation of the first astrophysical objects at Cosmic Dawn, a few hundred million years after the big bang ($z \gtrsim 15$; Dayal & Ferrara 2018). In recent years, a consensus has been established that the ionizing radiation of star-forming galaxies at $6 \lesssim z \lesssim 10$ was likely responsible for reionizing the majority of hydrogen in the Universe (Robertson et al. 2015; Finkelstein et al. 2019; Naidu et al. 2020). The foundational observations favouring this timeline, on the one hand, are the optical-depth measurements inferred from the cosmic microwave background (e.g. Planck Collaboration VI 2020). These measurements suggest the fraction of neutral hydrogen (H I) within the intergalactic medium (IGM) approached $\bar{x}_{\mathrm{H\,I}} = 1/2$ – in other words,

reionization reached the halfway mark – when the age of the Universe was approximately 0.6 Gyr ($z \sim 8$). On the other hand, a highly effective observational probe focused on galaxies in the later stages of reionization ($z \lesssim 7$) comes in the form of the principal $2p \rightarrow 1s$ electronic transition of hydrogen, H I Lyman α (Ly α) with resonance wavelength $\lambda_{\mathrm{Ly}\alpha} = 1215.67$ Å (Partridge & Peebles 1967).

The sensitivity of Ly α as a tracer of the ionization state of gas in and around galaxies can be attributed to the vast number of hydrogen atoms in the Universe, combined with the Lorentzian wings that characterize the non-Gaussian absorption cross-section of neutral hydrogen (Dijkstra 2014). This leads to severe resonant scattering of Ly α photons travelling through the interstellar medium (ISM) and IGM, unless these media are very highly ionized (Gunn & Peterson 1965). Barring strong evolution in the mechanisms regulating internal Ly α production within and Ly α escape from galaxies, reionization should therefore cause heavy attenuation of Ly α emission in the IGM at sufficiently high redshifts (Furlanetto, Hernquist & Zaldarriaga

★ E-mail: joris.witstok@nbi.ku.dk (JW); rm665@cam.ac.uk (RM)

2004; Dijkstra 2014; Ouchi, Ono & Shibuya 2020). A swift decline in the fraction of Ly α emitting galaxies (LAEs) has indeed been confirmed beyond $z \gtrsim 6$ (Stark et al. 2010, 2017; Pentericci et al. 2011; Schenker et al. 2014; Tilvi et al. 2014), strongly supporting a significant evolution in the IGM neutral hydrogen fraction within the first billion years of cosmic time (Mason et al. 2018a, 2019; Tilvi et al. 2020; Whitler et al. 2020).

Similarly, Ly α absorption due to residual neutral hydrogen seen in quasar spectra points towards an increasingly neutral state of the IGM at high redshifts (see Fan, Bañados & Simcoe 2023 for a review). However, a small number of sightlines reveal the persistence of long 'dark gaps', representing large, neutral islands of gas, towards late times ($z \sim 5$), which is interpreted as evidence for inhomogeneous reionization (Becker et al. 2015; Kulkarni et al. 2019; Keating et al. 2020; Bosman et al. 2022). Conversely, the most densely populated environments in the Universe are therefore predicted to readily host large-scale ionized regions early on (e.g. Mason et al. 2018b; Leonova et al. 2022; Qin et al. 2022). Crucially, these first ionized 'bubbles' become transparent to Ly α emission (Weinberger et al. 2018; Endsley et al. 2021, 2022; Jung et al. 2022a, b), which in turn renders the most distant LAEs powerful observational probes of the earliest sites of reionization (Hu et al. 2021; Endsley & Stark 2022; Trapp, Furlanetto & Davies 2023; Lu et al. 2024).

Recently, the successful deployment of the long-awaited *JWST* (McElwain et al. 2023; Rigby et al. 2023), whose near-infrared imaging and spectroscopy capabilities are specifically aimed at finding and characterizing the earliest galaxies (Robertson 2022; Gardner et al. 2023), has reinvigorated the search for such systems. In particular, the *JWST*/Near-Infrared Spectrograph (NIRSpec; Jakobsen et al. 2022; Böker et al. 2023) has proven efficient at uncovering new populations of LAEs in the early Universe (Jones et al. 2024b; Jung et al. 2024; Napolitano et al. 2024; Whitler et al. 2024), which in combination with the *JWST*/Near-Infrared Camera (NIRCam; Rieke et al. 2023a) provides an invaluable view into the physical conditions in and around LAEs in the epoch of reionization (EoR; e.g. Saxena et al. 2023; Witten et al. 2024; Witstok et al. 2024b).

While observational efforts prior to *JWST* had already been reasonably successful in identifying several of the brightest $z > 7$ sources as LAEs (e.g. Ono et al. 2012; Finkelstein et al. 2013; Oesch et al. 2015; Roberts-Borsani et al. 2016), Ly α emission observed beyond $z \sim 8$ remained elusive (e.g. Laursen et al. 2019). The discovery of Ly α emission in two $z \approx 8.6$ galaxies in close vicinity, EGSY8p7 and EGS-z910-44164, were the only two significant detections reported by Zitrin et al. (2015) and Larson et al. (2022), respectively. Exploiting *JWST*/NIRSpec measurements from the Cosmic Evolution Early Release Science (CEERS) programme (ID 1345, PI: Finkelstein; Finkelstein et al. 2023), Tang et al. (2023) found systemic redshifts based on rest-frame optical lines of $z = 8.678$ for EGSY8p7 (CEERS-1019) and $z = 8.610$ for EGS-z910-44164 (CEERS-1029) and confirmed the presence of Ly α emission in EGSY8p7, though only yielding a tentative Ly α detection for EGS-z910-44164 (not recovered by a later analysis; Nakane et al. 2024).

Remarkably, however, the enigmatic galaxy GN-z11 (Oesch et al. 2016) soon after proved that Ly α emission can readily be observed out to $z = 10.6$ (Bunker et al. 2023; Scholtz et al. 2024). GN-z11 was recently eclipsed by the discovery of a galaxy with an exceptionally strong Ly α line at $z = 13.0$, JADES-GS-z13-1-LA (Witstok et al. 2024a), at a time when the Universe was a mere 300 Myr old and, most likely, the IGM was still highly neutral (Tang et al. 2024a). Although the latter does not strictly preclude us from observing Ly α emission from a theoretical point of view (Hayes & Scarlata 2023), it does starkly contrast with recent indications of extremely strong Ly α absorption among the population of very early galaxies ($z \gtrsim 9$) uncovered by *JWST* (D'Eugenio et al. 2024b; Hainline et al. 2024a; Heintz et al. 2024a, b). Empirically, the surprisingly early presence of LAEs therefore raises many questions on the mechanisms regulating its production and escape in the early Universe. Is the possible influence of an active galactic nucleus (AGN; Maiolino et al. 2024) a necessary condition to observe Ly α, by producing an excess of ionizing photons and high-velocity outflowing gas that facilitates the escape of Ly α? Or are these sources unique by virtue of being located in overdense environments, as is the case for GN-z11 (Tacchella et al. 2023b; Scholtz et al. 2024), which may accommodate a small ionized bubble enhancing Ly α transmission?

To address such questions, in this work we present a detailed investigation of three of the most distant ($z > 8$) reionization-era LAEs newly discovered by *JWST*, including a $z \approx 8.5$ LAE reported recently by Tang et al. (2024b). The outline of this work is as follows: in Section 2, we discuss the observations underlying this work, and Section 3 discusses our methods and analysis. The main findings are placed in the context of results in the literature in Section 4. Finally, we summarize our findings in Section 5. We adopt a flat ΛCDM cosmology based on the latest results of the Planck collaboration (i.e. $H_0 = 67.4 \, \text{km s}^{-1} \, \text{Mpc}^{-1}$, $\Omega_{\text{m}} = 0.315$, $\Omega_{\text{b}} = 0.0492$; Planck Collaboration VI 2020) and a cosmic hydrogen fraction of $f_{\text{H}} = 0.76$ throughout. On-sky separations of 1 arcsec and 1 arcmin at $z = 8.5$ hence correspond to 4.73 physical kpc (pkpc) and 0.284 physical Mpc (pMpc), respectively. Magnitudes are quoted in the AB system (Oke & Gunn 1983).

2 OBSERVATIONS

2.1 Data sets

The observations considered here were primarily obtained as part of the *JWST* Advanced Deep Extragalactic Survey (JADES; Eisenstein et al. 2023a), supplemented with other relevant *JWST* programmes. JADES is designed and carried out by a collaboration between the NIRCam and NIRSpec instrument science teams and encompasses *JWST* guaranteed time observations (GTO) programme IDs (PIDs) 1180 and 1181 (PI: Eisenstein) as well as 1210, 1286, and 1287 (PI: Luetzgendorf), all located within the Great Observatories Origins Deep Survey (GOODS) extragalactic legacy fields (Giavalisco et al. 2004) in the equatorial North (GOODS-N) and South (GOODS-S), the latter of which contains the Hubble Ultra Deep Field (HUDF; Beckwith et al. 2006).

In addition to extensive multiwavelength ancillary data in both fields, GOODS-S in particular benefits from publicly available NIRCam observations from JEMS, the *JWST* Extragalactic Medium-band Survey (PID 1963, PIs: Williams, Maseda & Tacchella; Williams et al. 2023). Moreover, the First Reionization Epoch Spectroscopic COmplete Survey (FRESCO; PID 1895, PI: Oesch) provides NIRCam imaging and wide-field slitless spectroscopy (WFSS) over both GOODS-N and GOODS-S (Oesch et al. 2023). As in Witstok et al. (2024b), we consider the WFSS observations taken as part of FRESCO to obtain a large sample of high-redshift galaxies within the JADES footprint that are spectroscopically confirmed via their [O III] $\lambda 5008$ Å emission at $6.8 < z < 8.9$. The WFSS data reduction routine is described in Sun et al. (2023), while Helton et al. (2024a) outline the emission-line identification algorithms (see also Witstok et al. 2024b). Finally, we complement our data set with a dedicated follow-up programme targeting the JADES Origins Field (contained within GOODS-S) in observations completed in Cycle 2 (PID 3215, PIs: Eisenstein & Maiolino; Eisenstein et al. 2023b).

We refer to Rieke et al. (2023b), Bunker et al. (2024), and D'Eugenio et al. (2024a) for details on the JADES survey strategy, data reduction, and first public release of high-level science products derived from the NIRCam and NIRSpec measurements, respectively. Additional data sets discussed above are folded into the current analysis after having been processed in a consistent manner. In this work, we mainly focus on the NIRSpec spectroscopy, for which we briefly outline the relevant details in the following.

2.2 NIRSpec data reduction

The primary NIRSpec targets in JADES were drawn from samples of high-redshift galaxy candidates selected in a combination of publicly available *Hubble Space Telescope* (*HST*) and NIRCam imaging (Bunker et al. 2024), for which multi-object spectroscopy was obtained in the micro-shutter array (MSA) mode (Ferruit et al. 2022). The spectral configurations considered here are the low-resolution PRISM/CLEAR ('PRISM' hereafter; resolving power $30 \lesssim R \lesssim 300$ over a wavelength range between 0.6 and 5.3 μm) and the medium-resolution grating-filter combinations G140M/F070LP, G235M/F170LP, and G395M/F290LP (collectively 'R1000 gratings', with resolving power $R \approx 1000$).

Within the JADES NIRSpec observing strategy, there are the DEEP tiers, in which a limited number of sources were observed with long exposure times (between 9.3 and 28 h in PRISM mode, depending on slit placement across three visits; R1000 gratings each collect a third of the PRISM integration time), whereas the MEDIUM tiers targeted larger numbers of sources with exposure times of a few hours in both the PRISM and R1000 configurations. Additionally, tier identifiers distinguish between the two fields (GN for GOODS-N and GS for GOODS-S) as well as between two types of target selection, specifically those tiers based solely on *HST* imaging (e.g. MEDIUM-HST-GN) and those where *JWST* imaging was available (e.g. DEEP-JWST-GS). The NIRSpec observations from PID 3215 consist of exposures totalling 53.2 h in the PRISM mode, 11.2 h in G140M/F070LP, and 33.6 h in G395M/F290LP, and are classified as the ULTRA-DEEP-GS-3215 tier.

The current analysis is based on version 3 of the data reduction pipelines that were developed between the ESA NIRSpec Science Operations Team and the NIRSpec GTO team, which has been discussed in several previous JADES works (e.g. D'Eugenio et al. 2024a) and will be described in more detail in a forthcoming paper (Carniani & NIRSpec GTO collaboration, in preparation). We applied path-loss corrections assuming a point-source light profiles, taking into account the intra-shutter location of the targets. Throughout this work, one-dimensional spectra are extracted from the central three pixels along the central micro-shutter to maximize signal-to-noise ratio (SNR) on relative spectroscopic measurements (based on flux ratios) for these compact sources, while integrated galaxy properties such as stellar mass are derived in combination with the photometry (Section 3.2) to account for any additional path losses in the three-pixel extracted spectroscopy.

While these losses are well corrected for in terms of the ultraviolet (UV) continuum, as seen from the excellent agreement in UV magnitudes measured by NIRCam and NIRSpec (with the exception of JADES-GS-z8-1-LA where the slit only captures approximately half of the galaxy; Section 3.3 and Fig. 6), we note Ly α emission is often found to be extended (Leclercq et al. 2017; Wisotzki et al. 2018; Kusakabe et al. 2022; Guo et al. 2024) and occasionally exhibits spatial offsets from the UV continuum (e.g. Claeyssens et al. 2022; Simmonds et al. 2023). In these cases, the applied path loss corrections are not optimized to retrieve all Ly α flux,

such that the equivalent widths (EWs) may, in reality, be slightly higher. However, we have verified that an alternative background subtraction scheme where only the two off-centre nodding positions are considered yields very similar results. Although there is some hint of Ly α emission being more extended than the UV continuum from the two-dimensional spectra (e.g. Fig. 2), this similarity suggests the extension is not significantly larger than the extent of the micro-shutters (0.46 arcsec along the nodding direction; Jakobsen et al. 2022) given that it would be expected to suffer from self-subtraction in the default three-nod scheme, which is further corroborated by the compact morphology of the LAEs in the *F*115*W* filter containing Ly α (discussed further in Section 3.2).

3 METHODS AND ANALYSIS

3.1 LAE sample

The various tiers of NIRSpec observations within JADES (including the ultra-deep spectra from PID 3215; Section 2.1) comprised a total of 4100 targets, all of which were visually inspected to yield 174 galaxies robustly confirmed to be at $z > 6$, shown as the parent sample in Fig. 1, out of which 36 have redshifts $z > 8$ (D'Eugenio et al. 2024a). Within the full JADES sample, approximately 30 LAEs at $z > 6$ were identified from PRISM data, with three $z > 8$ galaxies showing well-detected (SNR > 3) Ly α emission in the R1000 spectra. More detailed statistics on the fraction of LAEs within the wider galaxy population across cosmic time are presented in Jones et al. (2024a). An extraordinary LAE at $z = 13.0$, whose
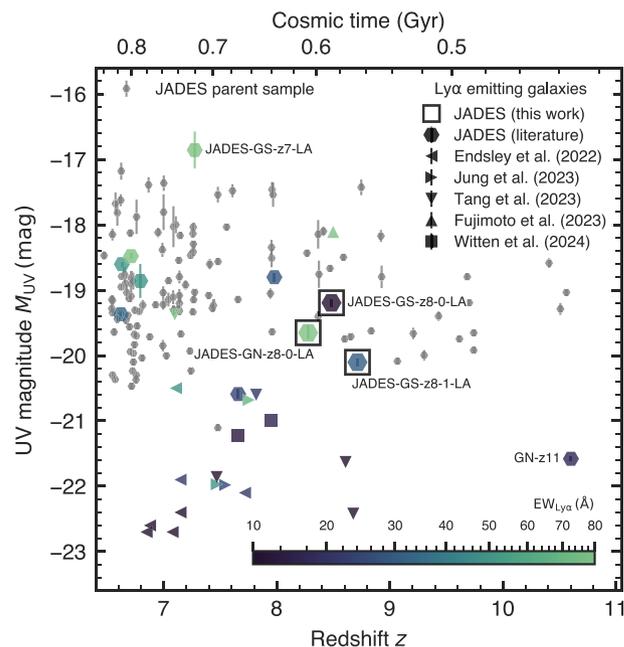

Figure 1. UV magnitudes, M_{UV}, of spectroscopically confirmed galaxies in the JADES parent sample (small grey points) as a function of cosmic time (D'Eugenio et al. 2024a). Distant LAEs ($z \gtrsim 6.5$) from the literature include JADES-GS-z7-LA (Saxena et al. 2023), GN-z11 (Bunker et al. 2023), as well as those samples compiled in Endsley et al. (2022), Jung et al. (2024), Tang et al. (2023), Fujimoto et al. (2023), Witten et al. (2024), and previous JADES works including Bunker et al. (2023), Jones et al. (2024b), Saxena et al. (2024), and Witstok et al. (2024b). Points are coloured according to the Ly α EW (colourbar on the right). The three sources studied in this work are highlighted with black squares.
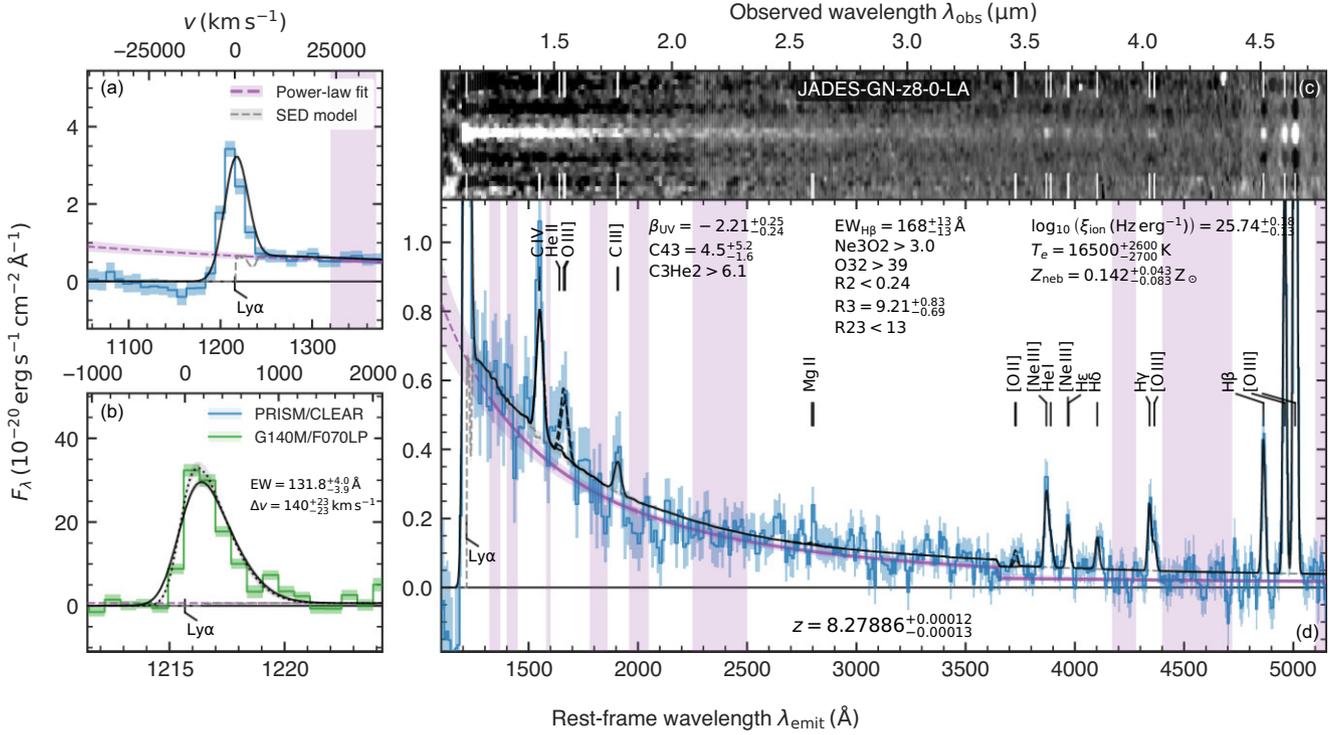
Figure 2. NIRSpec measurements of JADES-GN-z8-0-LA. The Ly α emission line is seen both in the low-resolution PRISM (panel a) and medium-resolution G140M/F070LP (panel b) spectra. The two-dimensional PRISM spectrum is shown in panel c, while panel d shows the one-dimensional spectrum extracted from a three-pixel aperture, both highlighting the locations of notable emission lines other than Ly α. A broken power law, fitted to line-free spectral regions in the rest-frame UV and optical (shaded light purple regions; see Table 1), is shown as a purple line in all panels (solid within the fitting range, dashed in the extrapolation). A grey dashed line shows the best-fitting SED model continuum (Section 3.2). An empirical emission-line fit, consisting of the latter with superimposed (asymmetric) Gaussian emission lines at the appropriate spectral resolution (Section 3.3), is shown by the solid black line. A dotted black line shows the unconvolved Ly α profile in panel b; dashed black lines in panel d indicate UV lines for which an upper limit is obtained (Section 3.3).

Ly α emission, however, is too faint to be seen in the R1000 spectrum, is discussed separately in Witstok et al. (2024a).

First, we consider JADES-GS + 53.15891-27.76508 (JADES-GS-z8-0-LAhereafter), the $z \simeq 8.49$ LAE discussed in Tang et al. (2024b). Originally, this source was identified as a Y_{105}-band dropout in *HST* imaging over the HUDF, placing its photometric redshift at $z_{phot} \approx 8.6$ (Bouwens et al. 2010; Bunker et al. 2010; McLure et al. 2010). Based on deep spectroscopy with the Spectrograph for INtegral Field Observations in the Near Infrared (SINFONI; Eisenhauer et al. 2003) on the Very Large Telescope (VLT), Lehnert et al. (2010) reported a 6σ detection of strong Ly α emission in this source at 1.16156 ± 0.00024 μm, implying $z_{Ly\alpha} = 8.5549 \pm 0.0002$, with a line flux of 6.1×10^{-18} erg s^{-1} cm^{-2} and an observed EW of 1900 Å (200 Å in the rest frame).

In PID 3215, JADES-GS-z8-0-LAwas one of six galaxies selected to be a sufficiently bright target for NIRSpec ($m \lesssim 30$ mag) with robust photometric redshift $8 < z_{phot} < 10$. Our new NIR-Spec observations confirm the source to be at a different redshift of $z \approx 8.48523 \pm 0.00006$, with Ly α emission lying more than ~ 2000 km s^{-1} bluewards of the claimed Lehnert et al. (2010) line (many times the spectral resolution of the NIRSpec grating and the SINFONI spectrograph). As will be discussed in Section 3.3, we measure a line flux of Ly α from NIRSpec to be 0.67×10^{-18} erg s^{-1} cm^{-2}, which is considerably lower ($\sim 10\times$) than for the line reported in Lehnert et al. (2010), and a rest-frame EW of 14.7Å (compared to 200Å in Lehnert et al. 2010). Hence, we conclude that the previously reported $z \approx 8.6$ line emission (Lehnert et al. 2010) is unlikely to be real (as we would have seen this at

an SNR > 50 in our NIRSpec spectrum), and indeed Bunker et al. (2013) argued this early detection was most likely to be spurious, as independent spectroscopic observations with VLT/FORS2 and Subaru/MOIRCS were not able to reproduce the feature. We note that the 2σ upper limit on the non-detection of the line flux of $F_{Ly\alpha} \approx 2 \times 10^{-18}$ erg s^{-1} cm^{-2} placed by Bunker et al. (2013) is fully consistent with our NIRSpec detection of faint Ly α flux 0.67×10^{-18} erg s^{-1} cm^{-2}.

Finally, our sample includes JADES-GN+189.19774 + 62.25696 (JADES-GN-z8-0-LA), which was placed on the MSA mask in the MEDIUM-HST-GN tier as one of 16 $z > 5.7$ galaxy candidates with $H_{160} < 27.5$ mag (photometric redshift $z_{phot} = 7.3$, priority class 2; cf. D'Eugenio et al. 2024a for details on the prioritization system in the MEDIUM tiers). The NIRSpec measurements revealed this to be an LAE with remarkably high EW at $z \simeq 8.28$, independently spectroscopically confirmed via [O III] λ 5008 Å in the FRESCO data (Helton et al. 2024a).[1] Finally, JADES-GS + 53.10900-27.90084 (JADES-GS-z8-1-LA), selected as a third priority class target among 13 other galaxies in the DEEP-JWST-GS tier, was found to be a third LAE at $z \simeq 8.72$. We summarize specific observational details for the three main LAEs in Table 2. Their observed PRISM and G140M/F070LP spectra are shown in Figs 2–4, while Fig. 5 shows their G395M/F290LP spectra.

---

[1]The FRESCO spectroscopy shows a marginal [O III] detection in JADES-GS-z8-0-LA, while JADES-GS-z8-1-LA falls outside the FRESCO footprint.
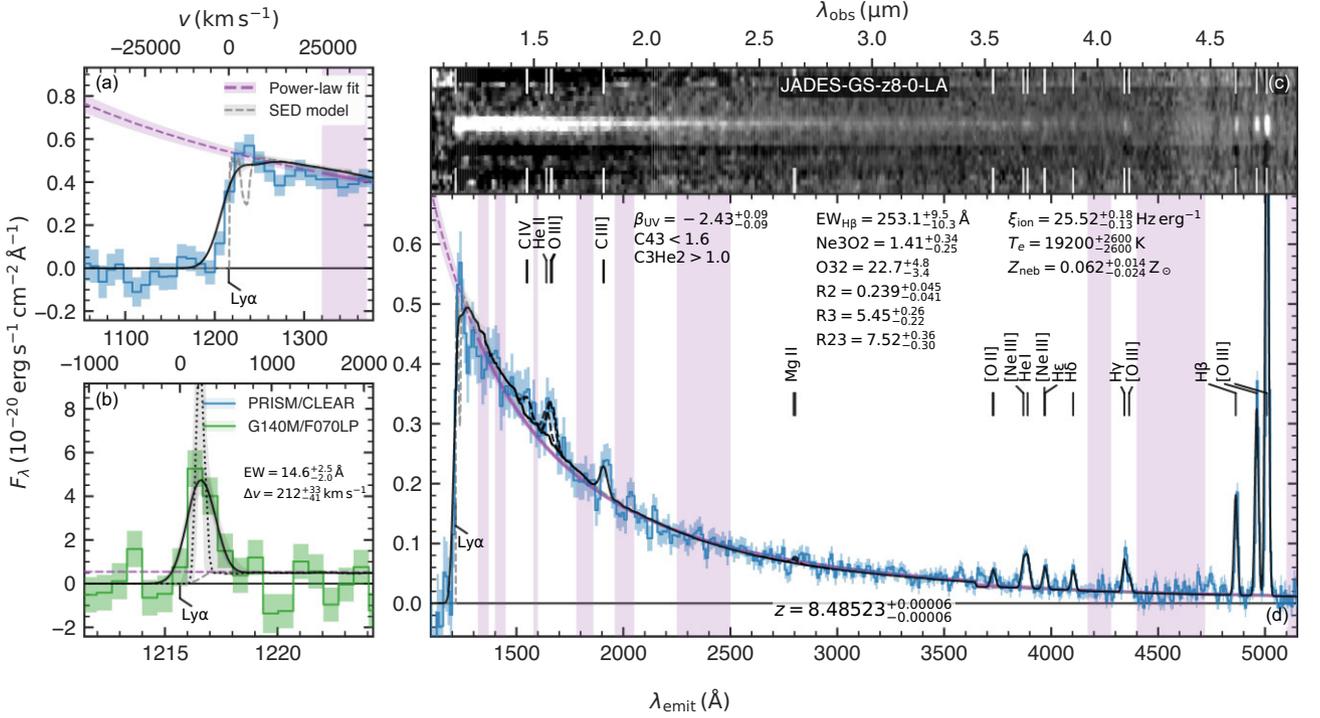
Figure 3. As Fig. 2, but for JADES-GS-z8-0-LA. The narrow Ly α line seen in the G140M/F070LP spectrum gets largely 'washed out' by the spectral break in the low-resolution PRISM spectrum (see e.g. Jones et al. 2024b).
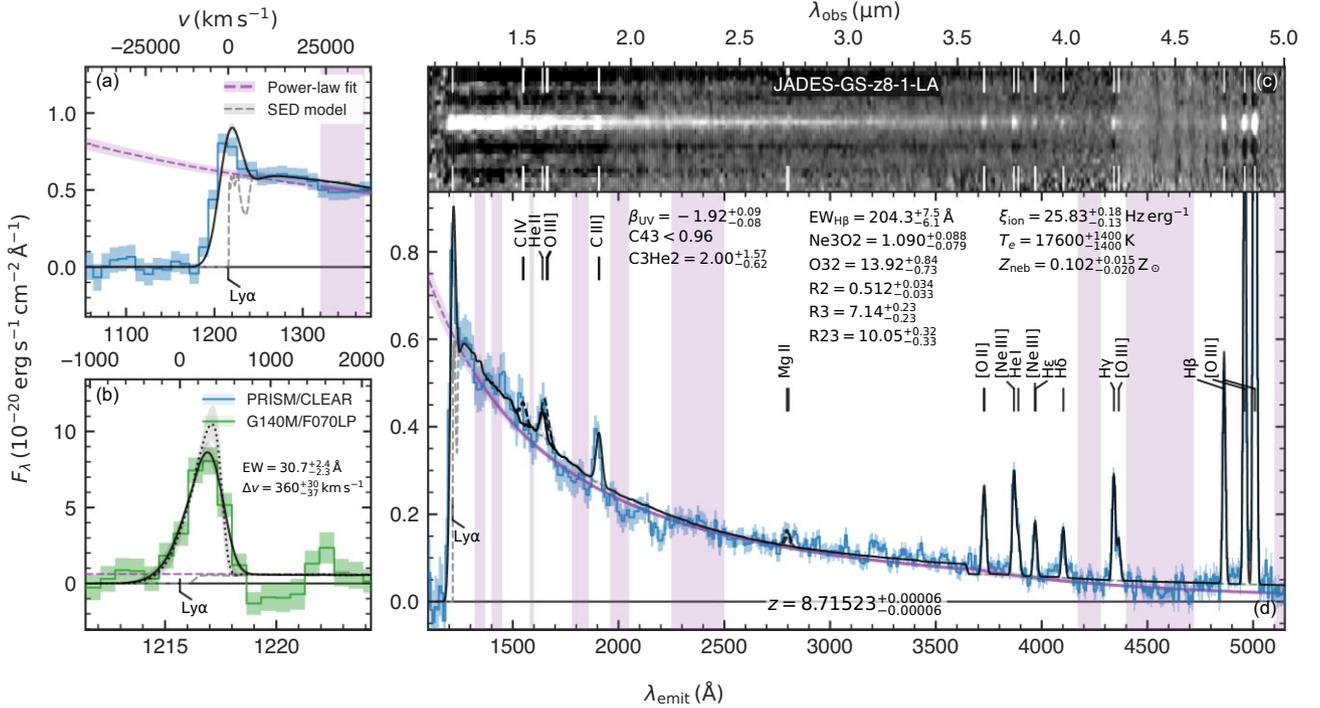

Figure 4. As Fig. 2, but for JADES-GS-z8-1-LA.

In the following, we discuss stellar population synthesis (SPS) modelling (Section 3.2) and further spectral fitting (Section 3.3), the results of which are summarized in Table 2. Specifically, we adopted a three-stage approach to model the available *JWST* spectroscopy and photometry. First, we determined the systemic redshift of each source based on several strong, well-detected, rest-frame optical emission lines (H δ, H γ, H β, [O III] λ 4960, 5008 Å) in the G395M/F290LP grating (Fig. 5) using the emission-line fitting routines described in Section 3.3. Secondly, we employed SPS models to infer the stellar and nebular properties from a combination of NIRSpec and NIRCam
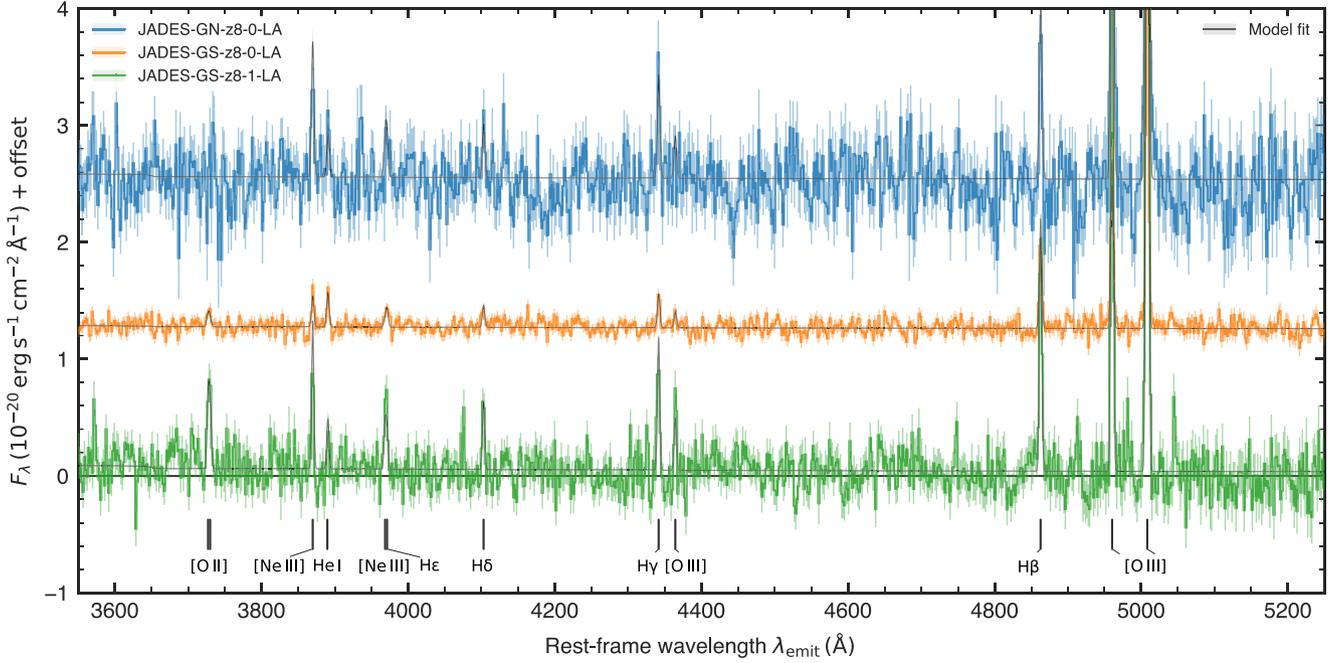
Figure 5. NIRSpec G395M/F290LP measurements of the three LAEs considered in this work, offset by 1.25 (2.5) $\times 10^{-20}$ erg s^{-1} cm^{-2} Å^{-1} in the case of JADES-GS-z8-0-LA (JADES-GS-z8-1-LA) for visualization purposes. The solid black line shows an empirical emission-line fit (see Section 3.3 for details).

measurements, discussed in more detail in Section 3.2. Finally, we performed a fitting routine of all observed emission lines in PRISM and R1000 gratings, taking into account the underlying continuum observed in the PRISM spectra (Section 3.3).

3.2 Stellar population synthesis modelling

NIRCam photometry was extracted from circular 0.3 arcsec-diameter apertures, except for JADES-GS-z8-1-LA where we performed full-scene modelling of the crowded field of sources with the FORCEPHO code (Johnson et al., in preparation) to obtain accurate photometry (see Appendix A for details). FORCEPHO simultaneously fits to the individual exposures in multiple photometric bands, using a single Sérsic (1963) light profile per source. To explore potential wavelength dependences in the morphology of all three LAEs, we additionally fit Sérsic profiles separately to the *F115W*, *F200W*, and *F444W* filters employing the PYSERSIC code (Pasha & Miller 2023). We do not find evidence for such wavelength dependence in any of the LAEs, however, with the three different filters yielding sizes fully consistent within the uncertainties. The resulting half-light radii found by PYSERSIC in *F200W*, probing rest-frame wavelengths around $\lambda_{emit} = 2000$ Å at $z \sim 8.5$, are reported as R_{UV} in Table 2.

We then modelled the full spectral energy distribution (SED) of the three LAEs combining the NIRSpec PRISM measurements (masking the spectral region around Ly α, 1150 Å $< \lambda_{emit} < 1280$ Å) and NIRCam photometry, largely following the methodology described in Witstok et al. (2023) and Looser et al. (2024). Briefly, we employed the Bayesian Analysis of Galaxies for Physical Inference and Parameter EStimation (BAGPIPES) code (Carnall et al. 2018) with Binary Population and Spectral Synthesis (BPASS) v2.2.1 models (Eldridge et al. 2017). We chose BPASS models that include binary stars and use the default BPASS initial mass function (IMF; stellar mass from 1 to 300 M$_\odot$ and slope of -2.35 for $M > 0.5$ M$_\odot$).

We assumed a non-parametric star formation history (SFH) under the prescription of Leja et al. (2019). Following Tacchella et al.

(2023a), we considered six bins in lookback time t, the first of which are located between 0 Myr $< t < 5$ Myr and 5 Myr $< t <$ 10 Myr, and the remaining four bins spaced logarithmically up until $t(z = 20)$. Logarithmic decrements in star formation rate (SFR) between adjacent bins, $x_i = \log_{10}(\text{SFR}_i/\text{SFR}_{i+1})$, are modelled using a Student's-t distribution with $\nu = 2$ degrees of freedom as a prior (Leja et al. 2019). We adopted a 'bursty-continuity' prior (Tacchella et al. 2022) where the scale is $\sigma = 1.0$, having verified a more smoothly varying SFH ($\sigma = 0.3$; 'standard continuity') yields consistent results. This flexible SFH accommodates stochastic star formation and underlying older stellar populations, both of which likely play an important role in the EoR (e.g. Whitler et al. 2023b; Looser et al. 2024), in a minimally biased framework weighing against very abrupt changes across SFH bins (e.g. Carnall et al. 2019b; Tacchella et al. 2022).

The total stellar mass formed and stellar metallicity were varied, respectively, across $0 < M_* < 10^{15}$ M$_\odot$, and 0.001 Z$_\odot < Z_* <$ 1.5 Z$_\odot$ (both log-uniform priors). We included nebular emission with freely varying ionization parameter ($-3 < \log_{10} U < -0.5$), which BAGPIPES derives from a grid of CLOUDY (Ferland et al. 2017) models computed self-consistently, with the relevant SPS models as incident radiation field and the nebular metallicity tied to that of the stars. A flexible Charlot & Fall (2000) prescription was included to model dust attenuation, with a Gaussian prior on the V-band attenuation ($\mu_{A_V} = 0.15$, $\sigma_{A_V} = 0.15$, limited to 0 mag $\leq A_V \leq 7$ mag) and the power-law slope over $0.4 < n < 1.5$, fixing the attenuation fraction arising from the diffuse ISM and stellar birth clouds to 40 per cent and 60 per cent, respectively (Chevallard et al. 2019). Finally, we assumed the spectroscopic data to follow the PRISM resolution curve of a uniformly illuminated micro-shutter,[2] and we allowed

---

[2]Provided by the Space Telescope Science Institute (STScI) as part of the *JWST* documentation: https://jwst-docs.stsci.edu/jwst-near-infrared-spectrograph/nirspec-instrumentation/nirspec-dispersers-and-filters.

them to be corrected by a first-order polynomial to take potential remaining aperture and flux calibration effects into account (Carnall et al. 2019a). The resulting best-fitting models are shown in Fig. 6.

From the NIRCam imaging, we identify several faint nearby sources (within 1.5 arcsec or ∼7 kpc) from which we extract NIRCam photometry in the same way as for the three main LAEs (see Fig. 6). While some are likely foreground galaxies (see Appendix A in particular), each LAE has one neighbouring source with photometry that appears consistent with being co-located in redshift (i.e. dropping out of the *F*090*W* filter). We fit the photometry of these neighbours fixing the redshift to that of the relevant LAE using the same methodology as described above (also shown in Fig. 6), the results of which are discussed in Appendix A.

3.3 Empirical fitting of continuum and line emission

Since continuum emission is not significantly detected in the R1000 measurements, we focused on the PRISM spectra to empirically determine the strength and shape of the continuum emission. To account for the potential presence of a discontinuity at the Balmer edge, $\lambda_{emit} = 3645.1$ Å, we separately fitted power-law continua ($F_\lambda \propto \lambda^\beta$) to line-free spectral regions in the rest-frame UV and optical. The rest-frame UV windows loosely follow those by Calzetti, Kinney & Storchi-Bergmann (1994), but given the limited spectral resolution of the PRISM, we merged several and avoided contamination by strong emission lines such as the C IV λ 1548, 1551 Å and [C III] λ 1907 Å, C III] λ 1909 Å (simply C III] hereafter) doublets, as summarized in Table 1. We find good agreement between the broken power law and the best-fitting BAGPIPES continua (consisting of a combination of stellar and nebular continuum; Section 3.2). Both indeed show evidence of Balmer 'jumps', suggestive of significant contribution of the nebular continuum (e.g. Cameron et al. 2024). We note there are some minor residuals between the model and observed continua (e.g. around C III] in the spectrum of JADES-GN-z8-0-LA; Fig. 2). However, these are largely within the estimated uncertainties and therefore can likely be attributed to noise fluctuations, corroborated by the good agreement seen in the other two sources (Figs 3 and 4), which received longer integration times (Table 2).

To measure the emission-line properties, we simultaneously fitted the PRISM and R1000 spectra with the best-fitting stellar continua as the underlying continuum in a Bayesian inference framework based on a PYTHON implementation of the MULTINEST multimodal nested-sampling algorithm (Feroz, Hobson & Bridges 2009), PYMULTINEST (Buchner et al. 2014).[3] We adopted a lognormal prior on the velocity dispersion such that $x = \log_{10} \sigma_v$ (km s^{-1}) is normally distributed with $\mu_x = \log_{10}(75)$ and $\sigma_x = 0.2$. Since the NIRSpec instrument possesses a point spread function (PSF) that is typically smaller than the width of a micro-shutter (0.2 arcsec; Jakobsen et al. 2022), its spectral resolution for compact sources can be significantly enhanced relative to the 'nominal' STScI resolution curves based on a uniformly illuminated micro-shutter (De Graaff et al. 2024). To account for this effect, we allowed the nominal STScI resolution curves based on a uniformly illuminated micro-shutter (Section 3.2) to be multiplied by a common scaling factor linear in wavelength (independent of the grating-filter combination). Motivated by the findings of De Graaff et al. (2024), we let this scaling factor vary uniformly from unity up to a factor of 2 and 1.6 at the blue and red ends of the NIRSpec wavelength coverage, 0.6 and 5.3 μm, respectively (Section 2.2).

We fitted Gaussian profiles to the rest-frame UV C IV λ 1548, 1551 Å, He II λ 1640 Å (He II), O III] λ 1660, 1666 Å, [C III] λ 1907 Å, C III] λ 1909 Å, and Mg II λ 2796, 2804 Å lines, the rest-frame optical [O II] 3727, 3730 Å, [Ne III] λ 3870 Å, He I λ 3890 Å, [Ne III] λ 3969 Å, [O III] λ 4364 Å, and [O III] λ 4960, 5008 Å lines, and the H I Balmer lines from Hβ down to Hε. We fixed line ratios set by atomic physics between the [Ne III] lines at 3870 and 3969 Å ($F_{3870}/F_{3969} = 3.319$), and between the [O III] lines at 4960 and 5008 Å ($F_{5008}/F_{4960} = 2.98$ as calculated in PYNEB; Luridiana, Morisset & Shaw 2015). If well detected, we varied the C III] doublet ratio between $0 < F_{1907}/F_{1909} < 1.7$ (Kewley et al. 2019) and the [O II] doublet ratio between $0.685 < F_{3727}/F_{3730} < 3.0$ (Sanders et al. 2016). Otherwise, a log-uniform distribution over 10^{-22} to 10^{-16} erg s^{-1} cm^{-2} was adopted for the integrated emission-line fluxes.

Meanwhile, Ly α was fit simultaneously in the PRISM and R1000 spectra as a skewed Gaussian profile[4] with full convolution of the continuum and line emission with the line spread function (LSF), to properly account for the smoothed continuum break in the low-resolution PRISM spectra (see Jones et al. 2024b for details). We take the peak of the profile to be the Ly α velocity offset from the systemic redshift, $\Delta v_{Ly\alpha}$. We adopted uniform priors on the velocity offset from the systemic redshift (Section 3.1), -500 km s^{-1} < $\Delta v_{Ly\alpha}$ < 1000 km s^{-1}, and intrinsic line width, 5 km s^{-1} < $\sigma_{v, Ly\alpha}$ < 2000 km s^{-1}.

Where appropriate, upper limits were calculated over a spectral window three times the size of velocity dispersion by integrating the continuum-subtracted observed spectrum, if higher than zero, to which we added three times the standard deviation on the total flux (i.e. 3σ) across the same window (found by summing individual channel uncertainties in quadrature). Line EWs were computed over a spectral region spanning five times the velocity dispersion around the central wavelength, except for Ly α where we simply divided the integrated line flux by the median value of the continuum at 1216.5 Å < λ_{emit} < 1225 Å. We show the best-fitting models at PRISM resolution in Figs 2–4. Integrated fluxes, EWs, and other inferred properties of individual lines, as well as a detailed view of the observed rest-frame UV lines, are presented in Appendix C.

We note that the observed emission-line profiles occasionally appear to show minimal discrepancies between the PRISM and R1000 spectra, which is likely due to minor remaining wavelength and flux calibration issues (D'Eugenio et al. 2024a). Our measurement of the systemic redshifts of JADES-GN-z8-0-LAand JADES-GS-z8-0-LA, $z = 8.27886 \pm 0.00012$ and $z = 8.48523 \pm 0.00006$, are consistent (within $< 1.5\sigma$) with the values reported by Tang et al. (2024a) and Tang et al. (2024b), respectively, $z = 8.279$ and $z = 8.4858 \pm 0.0004$, which were obtained based on an independent data reduction. While the use of multiple high-SNR emission lines, in our case the well-detected H δ, H γ, H β, and [O III] λ 4960, 5008 Å emission lines (Section 3.1) or H β and [O III] λ 4960, 5008 Å lines in the case of Tang et al. (2024b), allow a common line-centre measurement precision below the spectral pixel size of the G395M/F290LP grating ($\Delta\lambda_{obs} \approx 18$ Å or $\Delta z_{[O III]} \approx 0.0036$), the minor calibration issues not captured by the statistical uncertainty likely explain residual marginal differences.

---

[3]Code available at https://github.com/joriswitstok/emission_line_fitting.

[4]We opted to model the line profile as a skew-normal distribution (Azzalini & Capitanio 2009) to ensure its normalization is well defined.
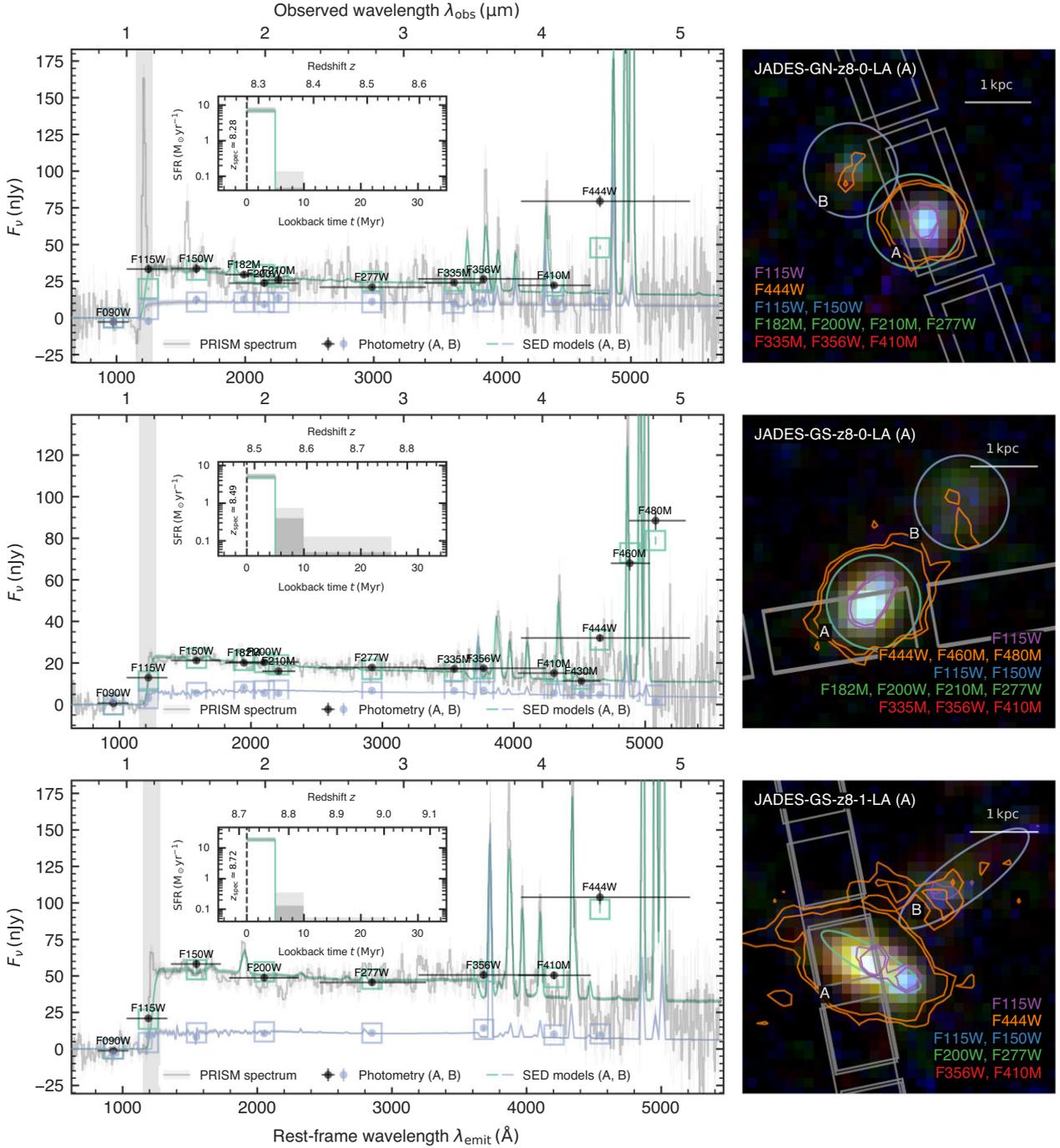
Figure 6. SED models of the three LAEs considered in this work, JADES-GN-z8-0-LA (top row), JADES-GS-z8-0-LA (middle row), and JADES-GS-z8-1-LA (bottom row). *Left column*: the low-resolution NIRSpec/PRISM spectra (light-grey line, with correction applied; see Section 3.2) and NIRCam photometry of the main sources (black points). Throughout, best-fitting BAGPIPES models are shown by cyan lines (dark and lighter shading representing 1σ and 2σ uncertainty), with open cyan squares indicating the predicted photometric data points. Photometry and accompanying SED models of neighbouring sources (B) are shown in blue. Inset panels show the modelled SFHs. *Right column*: false-colour images (North up, East left) created from stacks of available NIRCam filters as annotated (all convolved by 0.04 arcsec). The *F*115*W* image, into which Ly α is redshifted for all three LAEs, is overlaid in purple contours representing 3σ and 4σ. Similarly, orange contours show filters boosted by strong rest-frame optical lines (*F*444*W*, *F*460*M*, *F*480*M*). The placement of the NIRSpec micro-shutters is indicated by thin grey rectangles. Ellipses indicate the apertures from which the photometric data points are extracted (circular apertures 0.3 arcsec in diameter, except for JADES-GS-z8-1-LA). A scale bar in the top right shows the projected size of 1 kpc.

Table 1. Rest-frame wavelength windows for continuum measurements.

UV	Optical
$\lambda_{\rm emit}$ (Å)	
1320−1370	4170−4280
1400−1450	4400−4720
1580−1600	5100−5300
1780−1860	
1960−2050	
2250−2500	

4 DISCUSSION

4.1 Nebular properties

4.1.1 Dust attenuation

The observed strengths of the Balmer lines Hγ, Hδ, and Hε relative to Hβ are shown in Fig. 7. We compare these values with the theoretically predicted case-A and case-B line ratios, as computed in CLOUDY v23.01 (Ferland et al. 2017; Chatzikos et al. 2023), under physical conditions typical of H II regions (electron density $n_e = 300\,{\rm cm^{-3}}$ and temperature of $T_e = 15000\,{\rm K}$, motivated by the directly measured value; Section 4.1.3). Given the short spectral baselines between the Hβ and subsequent Balmer lines, we conclude that we cannot determine a very accurate measure of the attenuation, noting that even at higher SNR, a spread in Balmer decrements is observed with a non-negligible fraction of galaxies showing 'negative' (i.e. strictly unphysical) decrements (e.g. Reddy et al. 2015). Still, the observed line ratios, particularly those of Hδ and Hε spanning a longer wavelength range, are consistent within 1σ uncertainties with the intrinsic case-B ratios (except for Hγ in JADES-GS-z8-0-LA at $\sim 2\sigma$). This indicates little to no dust attenuation, in line with the observed blue UV slopes ($\beta_{\rm UV} \lesssim -2$) and as would be expected for galaxies with considerable Ly α escape fractions (e.g. Hayes et al. 2011). In the following, we will therefore conservatively set $A_V = 0.1$ mag to apply the appropriate dust-attenuation corrections, which we based on the average Small Magellanic Cloud (SMC) attenuation curve presented by Gordon et al. (2003).

4.1.2 Production and escape of ionizing photons

The efficiency with which stellar populations or AGN produce ionizing photons is commonly quantified as $\xi_{\rm ion} \equiv \dot{N}_{\rm ion}/L_{\nu,\,{\rm UV}}$, where $\dot{N}_{\rm ion}$ is the rate at which hydrogen-ionizing photons are emitted and $L_{\nu,\,{\rm UV}}$ is the UV luminosity density. We determine this quantity through the standard procedure (e.g. Stefanon et al. 2022; Saxena et al. 2023, 2024), measuring the UV luminosity density at a rest-frame frequency of $\nu_{\rm emit} = 1.999\,{\rm PHz}$ (i.e. $\lambda_{\rm emit} = 1500\,{\rm Å}$), and taking the luminosity of one of the hydrogen recombination lines (in this case Hβ) as a proxy for the rate of ionizing photons (Osterbrock & Ferland 2006), having applied a dust correction to both. Again assuming physical conditions typical of H II regions ($T_e = 15000\,{\rm K}$ and $n_e = 300\,{\rm cm^{-3}}$; Section 4.1.1), the conversion between Hβ luminosity $L_{\rm H\beta}$ and $\dot{N}_{\rm ion}$ is given by

$$\dot{N}_{\rm ion} = \frac{5.72 \times 10^{12}\,{\rm erg^{-1}}}{1 - f_{\rm esc,\,LyC}} L_{\rm H\beta} \quad \text{(case A)}, \tag{1}$$

$$\dot{N}_{\rm ion} = \frac{2.11 \times 10^{12}\,{\rm erg^{-1}}}{1 - f_{\rm esc,\,LyC}} L_{\rm H\beta} \quad \text{(case B)}, \tag{2}$$

where $f_{\rm esc,\,LyC}$ is the escape fraction of Lyman-continuum (LyC) photons. In the following, we will adopt the conversion given by equation (2), noting that case A instead would imply that $\dot{N}_{\rm ion}$ (and hence $\xi_{\rm ion}$) increases by $\sim 0.4\,{\rm dex}$.

Following convention in literature studies (e.g. Prieto-Lyon et al. 2023; Simmonds et al. 2023; Pahl et al. 2024), we set $f_{\rm esc,\,LyC} = 0$ for this calculation to derive $\xi_{\rm ion,\,0}$, where the subscript underlines it refers to the rate of non-escaping ionizing photons $\dot{N}_{\rm ion}(1 - f_{\rm esc,\,LyC})$, also considering that significant deviation from this scenario would likely violate pure case-B theory where the gas is assumed to be optically thick to LyC radiation (cf. McClymont et al. 2024). In reality, we may, however, expect $f_{\rm esc,\,LyC} \neq 0$ to explain the likely presence of ionized regions around the current sample of $z > 8$ LAEs (as will be discussed in Section 4.3.2), in which case our $\xi_{\rm ion,\,0}$ estimates effectively represent a lower limit for their true intrinsic value $\xi_{\rm ion}$. Nevertheless, we will argue in the following this calculation still yields a robust and useful estimate of the production efficiency of ionizing photons.

As the IGM prevents direct measurements of LyC photons above $z \gtrsim 4$ (Inoue et al. 2014), the LyC escape fraction is inherently unknown and notoriously hard to estimate for reionization-era galaxies. Still, given the combined EW of the [O III] and Hβ lines is observed to be $\sim 3 \times$ higher than the median value found in similarly bright ($M_{\rm UV} \approx -20\,{\rm mag}$) galaxies at $z \sim 8$ (Endsley et al. 2024), we conclude that in any case $f_{\rm esc,\,LyC}$ is unlikely to be extremely high, in which case the strengths of these lines would become suppressed. Indeed, based on the multivariate predictor developed by Choustikov et al. (2024), we indirectly estimate this quantity may range from 1 per cent to 3 per cent among the current sample of $z > 8$ LAEs, while according to the relation between UV slope and $f_{\rm esc,\,LyC}$ proposed by Chisholm et al. (2022) it ranges between 3 per cent and 10 per cent. Even at the highest value among these ($f_{\rm esc,\,LyC} = 10$ per cent), $\xi_{\rm ion}$ would only increase by approximately $\sim 0.05\,{\rm dex}$ relative to $\xi_{\rm ion,\,0}$.

The intrinsic Ly α and Hβ luminosities for case-B recombination under the same physical conditions as stated above are related as $L_{\rm Ly\alpha}/L_{\rm H\beta} = 23.48$ (34.00 for case A). This can be used to estimate the Ly α escape fraction $f_{\rm esc,\,Ly\alpha}$, the observed fraction of Ly α flux which is intrinsically produced in H II regions. We derived $f_{\rm esc,\,Ly\alpha}$ as the dust-corrected flux ratio of Ly α to Hβ divided by the theoretical intrinsic ratio in both case A and B (e.g. Saxena et al. 2023, 2024; Tang et al. 2023, 2024b).

All inferred quantities are summarized in Table 2. The directly measured values of $\xi_{\rm ion,\,0} \gtrsim 10^{25.4}\,{\rm Hz\,erg^{-1}}$ are $> 1.5 \times$ higher than reported values among statistical samples of EoR galaxies (Pahl et al. 2024; Simmonds et al. 2024), which match the canonical value, $10^{25.2}\,{\rm Hz\,erg^{-1}}$ (Robertson et al. 2015). Particularly JADES-GS-z8-1-LA is a proficient producer of ionizing photons, $\log_{10}(\xi_{\rm ion,\,0}\,({\rm Hz\,erg^{-1}})) = 25.67^{+0.18}_{-0.13}$, reminiscent of values recently inferred for the faint $6 < z < 7$ galaxy population ($M_{\rm UV} \gtrsim -17\,{\rm mag}$; Atek et al. 2024) even if JADES-GS-z8-1-LA is substantially brighter ($> 15 \times$). This source, however, like JADES-GS-z8-0-LA does not exhibit overly efficient Ly α escape, $f_{\rm esc,\,Ly\alpha} \approx 10$ per cent, in stark contrast with JADES-GN-z8-0-LA, for which we infer a large escape fraction of $f_{\rm esc,\,Ly\alpha} = 72 \pm 6$ per cent (case B) despite the IGM attenuation that may be expected to be rather large.

4.1.3 Ionization, excitation, and metal enrichment of the ISM

We define several commonly studied line-ratio diagnostics (e.g. Cameron et al. 2023b; Scholtz et al. 2023) across the rest-frame

Table 2. Sources studied in this work: observational details and measured and derived properties from a combination of NIRCam and NIRSpec.

General		JADES-GN-z8-0-LA	JADES-GS-z8-0-LA	JADES-GS-z8-1-LA
	NIRSpec ID	1899	20 213 084	20006347
	NIRCam ID	1 010 260	213 084	6347
	α_{2000} (deg)	189.197740	53.158906	53.109000
	δ_{2000} (deg)	62.256964	-27.765076	-27.900842
	NIRSpec tier	MEDIUM-HST-GN	ULTRA-DEEP-GS-3215	DEEP-JWST-GS
	Date of obs.	7 February 2023	16 October 2023	10 January 2024
	$t_{\rm exp,\,PRISM}$ (h)	2.9	53.2	18.7
	$t_{\rm exp,\,R1000}$ (h)	3×1.7	11.2 (G140M), 33.6 (G395M)	3×4.7
	$z_{\rm spec}$	$8.27886^{+0.00012}_{-0.00013}$	$8.48523^{+0.00006}_{-0.00006}$	$8.71523^{+0.00006}_{-0.00006}$
Stellar populations				
NIRCam and NIRSpec	M_* ($10^7\,{\rm M}_\odot$)	$3.48^{+0.56}_{-0.40}$	$2.58^{+0.49}_{-0.30}$	$9.22^{+1.40}_{-1.04}$
	Z_* ($10^7\,{\rm Z}_\odot$)	$0.14^{+0.01}_{-0.02}$	$0.12^{+0.03}_{-0.02}$	$0.15^{+0.01}_{-0.01}$
	SFR_{10} (${\rm M}_\odot\,{\rm yr}^{-1}$)	$3.52^{+0.56}_{-0.42}$	$2.57^{+0.36}_{-0.29}$	$9.36^{+1.36}_{-1.03}$
	$\Sigma_{\mathrm{SFR},\,10}$ (${\rm M}_\odot\,{\rm yr}^{-1}\,{\rm kpc}^{-2}$)	69.2 ± 26.6	1.88 ± 0.34	4.45 ± 1.05
	sSFR_{10} (${\rm Gyr}^{-1}$)	$101.84^{+0.10}_{-1.72}$	$101.43^{+0.54}_{-7.70}$	$101.88^{+0.08}_{-1.52}$
	t_* (Myr)	$2.75^{+2.07}_{-0.15}$	$3.43^{+8.22}_{-0.81}$	$2.70^{+2.19}_{-0.10}$
	A_V (mag)	$0.13^{+0.08}_{-0.06}$	$0.12^{+0.06}_{-0.06}$	$0.28^{+0.08}_{-0.08}$
	$\log_{10} U$	$-1.09^{+0.13}_{-0.20}$	$-0.81^{+0.18}_{-0.21}$	$-1.40^{+0.12}_{-0.09}$
Rest-frame UV				
NIRCam (F150W)	$M_{\rm UV}$ (mag)	-19.65 ± 0.10	-19.19 ± 0.05	-20.33 ± 0.05
NIRCam (F200W)	$R_{\rm UV}$ (pc)	90 ± 10	466 ± 30	579 ± 50
NIRSpec	$M_{\rm UV}$ (mag)	$-19.41^{+0.09}_{-0.08}$	$-19.23^{+0.03}_{-0.03}$	$-19.57^{+0.03}_{-0.03}$
	$\beta_{\rm UV}$	$-2.21^{+0.25}_{-0.24}$	$-2.43^{+0.09}_{-0.09}$	$-1.92^{+0.09}_{-0.08}$
	$\mathrm{EW}_{\rm Ly\alpha}$ (Å)	$131.8^{+4.0}_{-3.9}$	$14.6^{+2.5}_{-2.0}$	$30.7^{+2.4}_{-2.3}$
	$\Delta v_{\rm Ly\alpha}$ (km s^{-1})	140^{+23}_{-23}	212^{+33}_{-41}	360^{+30}_{-37}
	$f_{\rm esc,\,Ly\alpha}$ (case A)	$0.494^{+0.044}_{-0.041}$	$0.089^{+0.016}_{-0.013}$	$0.0841^{+0.0071}_{-0.0069}$
	$f_{\rm esc,\,Ly\alpha}$ (case B)	$0.715^{+0.063}_{-0.060}$	$0.129^{+0.022}_{-0.018}$	$0.122^{+0.010}_{-0.010}$
	C43	$4.5^{+5.2}_{-1.6}$	< 1.6	< 0.96
	C3He2	> 6.1	> 1.0	$2.00^{+1.57}_{-0.62}$
Rest-frame optical				
NIRSpec	$\mathrm{EW}_{\rm H\beta}$ (Å)	168^{+13}_{-13}	$253.1^{+9.5}_{-10.3}$	$204.3^{+7.5}_{-6.1}$
	$\mathrm{EW}_{[\mathrm{O\,III}]\lambda 4960\,\text{Å}}$ (Å)	$525.5^{+7.7}_{-8.1}$	$479.8^{+4.9}_{-4.2}$	$505.5^{+3.5}_{-3.5}$
	$\mathrm{EW}_{[\mathrm{O\,III}]\lambda 5008\,\text{Å}}$ (Å)	1600^{+24}_{-25}	1479^{+15}_{-13}	1534^{+10}_{-10}
	Ne3O2	> 3.0	$1.41^{+0.34}_{-0.25}$	$1.090^{+0.088}_{-0.079}$
	O32	> 39	$22.7^{+4.8}_{-3.4}$	$13.92^{+0.84}_{-0.73}$
	R2	< 0.24	$0.239^{+0.045}_{-0.041}$	$0.512^{+0.034}_{-0.033}$
	R3	$9.21^{+0.83}_{-0.69}$	$5.45^{+0.26}_{-0.22}$	$7.14^{+0.23}_{-0.23}$
	R23	< 13	$7.52^{+0.36}_{-0.30}$	$10.05^{+0.32}_{-0.33}$
	$\log_{10} \left(\xi_{\rm ion,\,0}\,(\mathrm{Hz\,erg}^{-1}) \right)$	$25.58^{+0.18}_{-0.13}$	$25.37^{+0.18}_{-0.13}$	$25.67^{+0.18}_{-0.13}$
	T_e (K)	16500^{+2600}_{-2700}	19200^{+2600}_{-2600}	17600^{+1400}_{-1400}
	$12 + \log_{10}(\mathrm{O/H})$	$7.84^{+0.11}_{-0.38}$	$7.481^{+0.089}_{-0.209}$	$7.699^{+0.059}_{-0.097}$
	$Z_{\rm neb}$ (${\rm Z}_\odot$)	$0.142^{+0.043}_{-0.083}$	$0.062^{+0.014}_{-0.024}$	$0.102^{+0.015}_{-0.020}$

Note. Listed general properties are the NIRSpec and NIRCam IDs, right ascension (α_{2000}) and declination (δ_{2000}), NIRSpec tier, date the NIRSpec observations were taken, exposure times ($t_{\rm exp}$) in the PRISM and R1000 modes, and photometric and spectroscopic redshifts ($z_{\rm phot}$ and $z_{\rm spec}$). Stellar population properties (Section 3.2) include the stellar mass (M_*), stellar metallicity (Z_*), (specific) SFR and its surface density averaged over the last 10 Myr, (s)SFR$_{10}$ and $\Sigma_{\mathrm{SFR},\,10}$, mass-weighted stellar age (t_*), V-band attenuation (A_V), and ionization parameter (U). Rest-frame UV properties are the absolute magnitude ($M_{\rm UV}$), deconvolved half-light radius ($R_{\rm UV}$), UV slope ($\beta_{\rm UV}$), Ly α equivalent width (EW$_{\rm Ly\alpha}$), Ly α velocity offset ($\Delta v_{\rm Ly\alpha}$), Ly α escape fraction ($f_{\rm esc,\,Ly\alpha}$) assuming case A and case B, and the C43 and C3He2 line ratios (see Section 4.1.3). Rest-frame optical properties are the EWs of the H β, [O III] λ 4960, 5008 Å lines (EW$_{\rm H\beta}$, EW$_{[\mathrm{O\,III}]\lambda 4960\,\text{Å}}$, EW$_{[\mathrm{O\,III}]\lambda 5008\,\text{Å}}$), the Ne3O2, O32, R2, R3, and R23 line ratios, the ionizing photon production efficiency ($\xi_{\rm ion,\,0}$), electron temperature (T_e), and the nebular oxygen abundance and metallicity ($12 + \log_{10}(\mathrm{O/H})$ and $Z_{\rm neb}$; Sections 4.1.3 and 4.1.2).
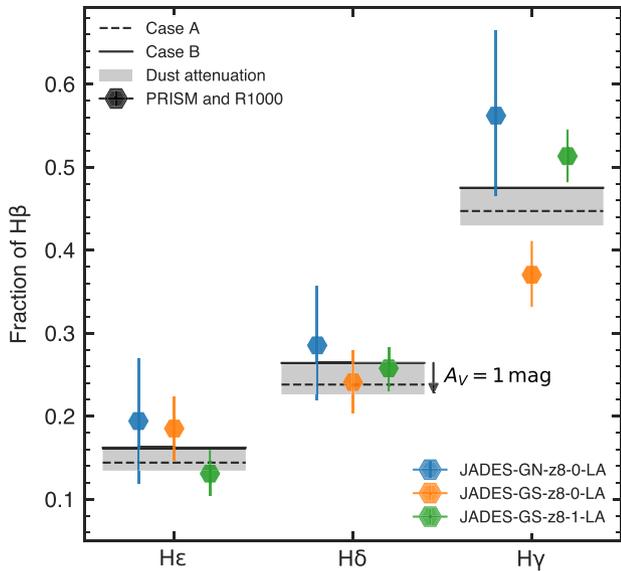
Figure 7. Observed Balmer line ratios, as measured in the PRISM and R1000 spectra, with respect to Hβ. Solid and dashed black lines represent the theoretical case-A and case-B values, respectively (Section 4.1.1), with grey shading indicating a shift from the case-B value caused by a corresponding *V*-band attenuation of $A_V = 1$ mag (assuming the SMC attenuation curve presented by Gordon et al. 2003). While an accurate measure of the attenuation is hindered by the uncertainties and small wavelength leverage, the observed line ratios (particularly those of Hδ and Hε) are broadly consistent with the intrinsic case-B ratios, indicating little to no dust attenuation.

UV and optical as

$$C43 = C\ \text{IV}\ \lambda\ 1548,\ 1551\,\text{Å}/C\ \text{III}],$$

$$C3He2 = C\ \text{III}]/He\ \text{II}\ \lambda\ 1640\,\text{Å},$$

$$Ne3O2 = [Ne\ \text{III}]\ \lambda\ 3870\,\text{Å}/[O\ \text{II}],$$

$$O32 = [O\ \text{III}]\ \lambda\ 5008\,\text{Å}/[O\ \text{II}],$$

$$R2 = [O\ \text{II}]/H\beta,$$

$$R3 = [O\ \text{III}]\ \lambda\ 5008\,\text{Å}/H\beta,$$

$$R23 = [O\ \text{II}] + [O\ \text{III}]\ \lambda\ 4960,\ 5008\,\text{Å}/H\beta,$$

where the line labels represent the corresponding integrated fluxes, and C III] and [O II] are shorthand, respectively, for the [C III] λ 1907 Å, C III] λ 1909 Å and [O II] λ 3727, 3730 Å doublets.

We detect the auroral [O III] λ 4364 Å line in all three LAEs, which allows us to constrain the electron temperature T_e and estimate the oxygen abundance via the direct method (Curti et al. 2020, 2023; Sanders et al. 2023, 2024). The strength of this transition, which corresponds to the $2s^2\ 2p^2\ ^1S_0 \rightarrow 2s^2\ 2p^2\ ^1D_2$ transition of O^{2+}, is highly dependent on collisional excitation that populates the upper ($^1S_0$) level, so that the ratio of [O III] λ 4364 Å relative to the [O III] λ 5008 Å line ($2s^2\ 2p^2\ ^1D_2 \rightarrow 2s^2\ 2p^2\ ^3P_2$) is strongly positively correlated with the electron temperature T_e.

We employed the PYNEB code (Luridiana et al. 2015) to calculate temperatures and abundance ratios, adopting the electron impact excitation collision strengths from Pradhan et al. (2006) and Tayal (2007) for O^+, and those from Aggarwal & Keenan (1999) and Palay et al. (2012) for O^{2+}. We derived the oxygen abundance via the common approximation $O/H \approx O^+/H + O^{2+}/H$ (e.g. Laseter et al. 2024 and references therein), except for JADES-GN-z8-0-LA where we take $O/H \approx O^{2+}/H$ given the [O II] doublet is not detected, noting that O^{2+} typically dominates the oxygen budget in the low-

metallicity regime (Curti et al. 2017). We assumed the relation from Pilyugin et al. (2009) to derive the temperature of [O II]-emitting gas based on the O^{2+} temperature, $T_{O^+} = 0.835\ T_{O^{2+}} + 0.264$. We note there is likely some systematic bias in these estimates due to temperature fluctuations on the scale of individual H II regions (Marconi et al. 2024), which may cause the metallicity to be underestimated (Cameron, Katz & Rey 2023a). We quote gas-phase metallicities Z_{neb} adopting a solar oxygen abundance of $12 + \log_{10}(O/H)_\odot = 8.69$ (Asplund et al. 2009).

We infer via the direct-T_e method that the ISM in these LAEs is relatively hot ($T_e > 15000$ K), and is characterized by low (yet not extremely low) gas-phase metallicities of approximately 10 per cent solar, in agreement with the metallicities found in the SED modelling. As expected given these low metallicities and in line with previous work on LAEs (Maseda et al. 2020; Saxena et al. 2023; Simmonds et al. 2023), they are efficient at producing ionizing photons, $\xi_{ion,0} \gtrsim 10^{25.4}$ Hz erg^{-1} (Section 4.1.2). In the following sections, we will investigate which intrinsic sources of ionization are powering the strong nebular emission (Section 4.2.2), and which escape mechanisms are in place that allow the Ly α emission to be observable well into the EoR, including the potential role of environment (Section 4.3).

4.2 On the nature of primaeval LAEs

4.2.1 Stellar properties

The main results of the SPS modelling (Section 3.2), spectral fitting (Section 3.3), and derived physical quantities (Section 4.1) are shown in Table 2. While there are some hints of slightly more evolved underlying stellar populations (Fig. 6), we find that the observed photometry and spectroscopy of the LAEs studied here, when interpreted purely as stellar in its origin, is largely dominated by the light of very young ($t_* < 5$ Myr) and metal-poor ($Z_* \approx 0.15\,Z_\odot$) stars. Morphologically, each LAE is very compact: we measure deconvolved half-light radii (Section 3.2) of $R_{UV} \approx 500$ pc for JADES-GS-z8-0-LA and JADES-GS-z8-1-LA, and JADES-GN-z8-0-LA is smaller yet ($R_{UV} = 90 \pm 10$ pc). We note the *F115W* filter containing Ly α shows a consistently compact morphology (Section 3.2), in the case of JADES-GS-z8-1-LA even revealing two sources (Appendix A). Dominating the rest-frame UV, they are reminiscent of the compact, young star clusters that have recently begun to be resolved in gravitationally lensed, high-redshift galaxies by *JWST* and are speculated to form through gravitational instabilities in a more extended gaseous disc (Fujimoto et al. 2024) and be precursors to globular clusters (Adamo et al. 2024). Indeed, given the young stellar ages and little dust obscuration ($A_V < 0.3$ mag) inferred from the integrated SEDs, the comparatively UV-bright LAEs (relative to e.g. Saxena et al. 2023, 2024) are characterized by low mass-to-light ratios and thus relatively low stellar masses ($M_* < 10^8\,M_\odot$).

These stellar properties are reflected in the extreme nebular emission-line properties observed with NIRSpec. We find the optical lines to exhibit very large EWs of around EW$_{[O III]+ H\beta} \approx 2000$ Å, roughly $\sim 3\times$ higher than the median value found in similarly bright ($M_{UV} \approx -20$ mag) galaxies at $z \sim 8$ (Endsley et al. 2024). Such strong nebular line emission is indicative of high specific SFR (sSFR; Stark et al. 2013; Smit et al. 2014, 2015; Boyett et al. 2024; Tang et al. 2024c), as confirmed by the SED modelling (sSFR$_{10} \approx 100$ Gyr^{-1}). Assuming half of the inferred SFR is spread uniformly over πR_{UV}^2, the area enclosed by the half-light radius (e.g. Morishita et al. 2024), the compact sizes moreover imply high SFR surface densities of
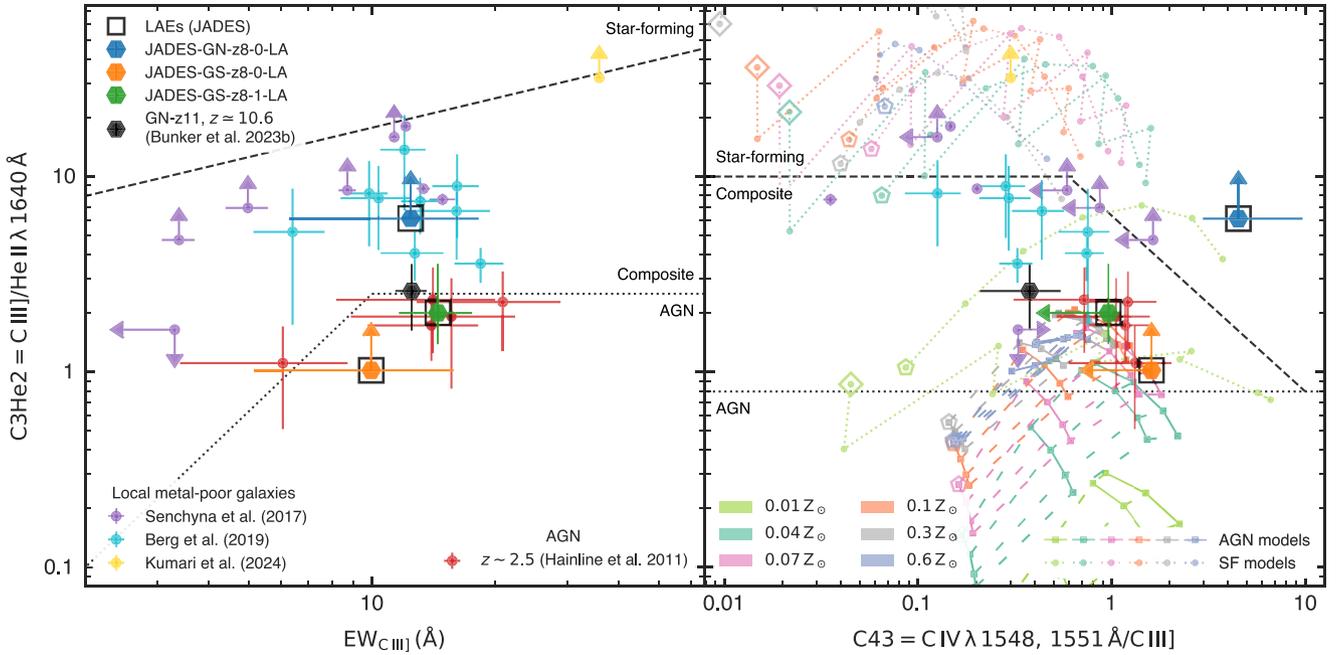
Figure 8. Rest-frame UV emission-line diagnostic diagrams from Hirschmann et al. (2019). The LAEs considered in this work are highlighted by coloured hexagons outlined by black squares. GN-z11 (Bunker et al. 2023) is shown by a black hexagon. In both panels, the dashed and dotted black lines were designed by Hirschmann et al. (2019) to separate star-forming galaxies from those with composite origin of the nebular emission (AGN and star formation), and composite from AGN, respectively. We include measurements based on UV spectroscopy of local metal-poor galaxies, shown as small purple, blue, and yellow circles (Senchyna et al. 2017; Berg et al. 2019; Kumari et al. 2024), and of $z \sim 2.5$ AGN (Hainline et al. 2011). *Left panel*: C3He2 ratio versus the EW of C III]. *Right panel*: C3He2 ratio versus C43 ratio. Models for the predicted line ratios with star formation (SF; small circles) and AGN (small squares) as ionizing sources are overplotted, with colours indicating varying metallicity according to the legend in the bottom left (see Section 4.2.2 for details). Starting from the larger open pentagons (Feltre et al. 2016; Gutkin et al. 2016) or diamonds (Nakajima & Maiolino 2022), the ionization parameter increases along the dotted or dashed lines. For AGN models, solid lines additionally show variation in the spectral power-law slope α. The emission-line properties of the $z > 8$ LAEs considered here can be explained as originating in star formation, except for JADES-GS-z8-1-LA at $z \simeq 8.72$ which shows evidence of photoionization by an AGN.

$\Sigma_{\mathrm{SFR}} > 1\,\mathrm{M}_\odot\,\mathrm{yr}^{-1}\,\mathrm{kpc}^{-2}$, in the case of JADES-GN-z8-0-LA even $\Sigma_{\mathrm{SFR}} \approx 80\,\mathrm{M}_\odot\,\mathrm{yr}^{-1}\,\mathrm{kpc}^{-2}$. Such intensely confined star formation is very rarely seen in local galaxies, but has been found to become the norm in reionization-era galaxies (Morishita et al. 2024), especially at the highest-redshift regime (Robertson et al. 2023; Castellano et al. 2024), perhaps paving the way to the early formation of dense stellar cores (e.g. Baker et al. 2024).

4.2.2 Sources of ionization

Traditionally, AGN activity has been diagnosed by determining whether specific optical line ratios fall within theoretical (Kewley et al. 2001) or empirical (Kauffmann et al. 2003) star-forming demarcations, specifically on the classification diagrams proposed by Baldwin, Phillips & Terlevich (1981, BPT) and Veilleux & Osterbrock (1987, VO87). While these diagnostic methods have been explored extensively and well calibrated for galaxies at $z \lesssim 3$ (Steidel et al. 2014), they become more challenging to employ in the high-redshift regime, in the first place because key optical lines shift out of the spectral coverage: even with NIRSpec, the Hα, [N II], and [S II] lines become inaccessible at $z \gtrsim 7$ (as is the case for the $z > 8$ LAEs considered here). Moreover, line ratios on the BPT and VO87 diagrams have been shown to significantly deviate from the sequences occupied by local star-forming galaxies and AGNs, and hence lose their discriminating power, in the low-metallicity regime (Harikane et al. 2023; Hirschmann et al. 2023; Scholtz et al. 2023; Übler et al. 2023; Calabro et al. 2024). We therefore

instead consider two diagnostic diagrams designed for rest-frame UV lines, proposed by Hirschmann et al. (2019) to distinguish between AGN and star formation over a range of redshift ($0 < z \lesssim 6$) based on the implementation of photoionization models in cosmological simulations.

The diagrams, consisting of the EW of the C III] doublet and the (dust-corrected) C3He2 and C43 line ratios, are displayed in Fig. 8. We show the three main LAEs alongside local, metal-poor galaxies (Senchyna et al. 2017; Berg et al. 2019), including Pox186 (Kumari et al. 2024), a dwarf galaxy that is observed to have one of the highest known EWs of C III] (34 Å) as well as the highest far-infrared [O III] 88 μm to [C II] 158 μm line ratio seen among local galaxies ([O III]/[C II] ≈ 10, comparable to what is typically seen in reionization-era galaxies; Witstok et al. 2022). Following Witstok et al. (2021a), we also directly compared the C3He2 and C43 ratios with the Gutkin, Charlot & Bruzual (2016) and Feltre, Charlot & Gutkin (2016) photoionization models computed in CLOUDY (Ferland et al. 2017) with star formation and AGN as ionizing sources, respectively. The star formation models are based on an updated version of the Bruzual & Charlot (2003) SPS models under a Chabrier (2003) IMF with an upper mass limit of $300\,\mathrm{M}_\odot$, and adopt a constant SFH over 100 Myr. We considered models with fixed dust-to-metal ratios, $\xi_{\mathrm{d}} = 0.3$, and hydrogen densities, $n_{\mathrm{H}} = 10^2\,\mathrm{cm}^{-3}$ for star formation models and $10^3\,\mathrm{cm}^{-3}$ for AGN (noting that varying these parameters does not significantly impact the results). We varied the ionization parameter ($-4 < \log_{10} U < -1$) and, for the narrow-line region AGN models, the power-law slope of the rest-

frame UV (i.e. $S_\nu \propto \nu^\alpha$ at $\lambda_{emit} \leq 2500\,\text{Å}$; see Feltre et al. [2016]), $-2 < \alpha < -1.2$. To convert absolute metallicities to solar units, we adopt $Z_\odot = 0.0134$ (Asplund et al. [2009]).

We complement the star formation photoionization models described above by the (regular, Population II) models from Nakajima & Maiolino ([2022]). While these are also based on CLOUDY (Ferland et al. [2017]) and explore a similar range of metallicity[5] and ionization parameter as discussed above, some parameters are tweaked to form a representative set of models specifically for galaxies in the very early Universe. A higher density of $n_H = 10^3\,\text{cm}^{-3}$ is adopted (see e.g. Sanders et al. [2016]), and the incident radiation field is instead set by a very young (1 Myr or 10 Myr) stellar population, as modelled by BPASS v2.2.1 (Eldridge et al. [2017]) under its default IMF ranging up to $300\,M_\odot$ (cf. Section [3.2]). To aid visualization in Fig. [8], we leave out the Nakajima & Maiolino ([2022]) AGN models here, noting these occupy broadly the same region in terms of C3He2 and C43 ratios as the Feltre et al. ([2016]) AGN models.

From this comparison, we find that JADES-GN-z8-0-LA shows nebular emission-line ratios consistent with what is expected for star formation in the metal-poor regime, both empirically (showing similarity to local metal-poor galaxies) and from the perspective of photoionization modelling. Interestingly, the high C43 line ratio is only reproduced under extreme circumstances (Topping et al. [2024]): it requires the highest ionization parameter ($\log_{10} U = -1$) in the Gutkin et al. ([2016]) model track that is significantly more metal poor (~ 1 per cent solar) than directly inferred (~ 15 per cent solar; Table [2]). This may be a result of the actual SFH rising very steeply over the last 10 Myr (while extending further back to account for the existing metal content), whereas the Gutkin et al. ([2016]) models adopt a constant SFH over 100 Myr. The Nakajima & Maiolino ([2022]) models similarly struggle to reproduce such a high C43 ratio, except for the most metal-poor track which, however, underpredicts the C3He2 ratio.

A lack of detections of the C IV and He II lines in JADES-GS-z8-0-LA prevents us from conclusively determining its main source of ionization, and although it is formally located in a region demarcating AGN activity, the upper limits indicate this galaxy could be consistent with star formation. Conversely, JADES-GS-z8-1-LA at $z \simeq 8.72$ shows a reasonably strong He II line at $EW_{He\,II} = 4.9^{+1.9}_{-2.0}\,\text{Å}$ (detected consistently between the PRISM and R1000 modes, though only at $\sim 3\sigma$; see Appendix [C]). Its emission-line ratios, similar to those measured in stacked spectra of $z \sim 2.5$ AGN (Hainline et al. [2011]), indicate the ionization source may be a combination of AGN and star formation, if not dominated by an AGN. This finding is corroborated by the high [O III] $\lambda 4364\,\text{Å}/H\gamma \approx 0.4$ ratio found in JADES-GS-z8-1-LA, typically only observed in AGN (Brinchmann [2023]; Mazzolari et al. [2024]; Übler et al. [2024]).

4.3 Ionized bubbles: driven by individual sources or in concert?

4.3.1 Comparing LAE properties across cosmic time

To gain insight into the mechanisms regulating the production and escape of Ly α in reionization-era LAEs ($z \gtrsim 6$), in Fig. [9], we compare their Ly α EWs to those of LAEs at lower redshift, where the impact of IGM absorption of Ly α is minimal, while controlling for the effective ionization parameter by means of the O32 ratio or for the

---

[5]Since the exact metallicities in Nakajima & Maiolino ([2022]) differ slightly from those in Gutkin et al. ([2016]) and Feltre et al. ([2016]) models, for simplicity we use the values that match the rounded values shown in Fig. [8].
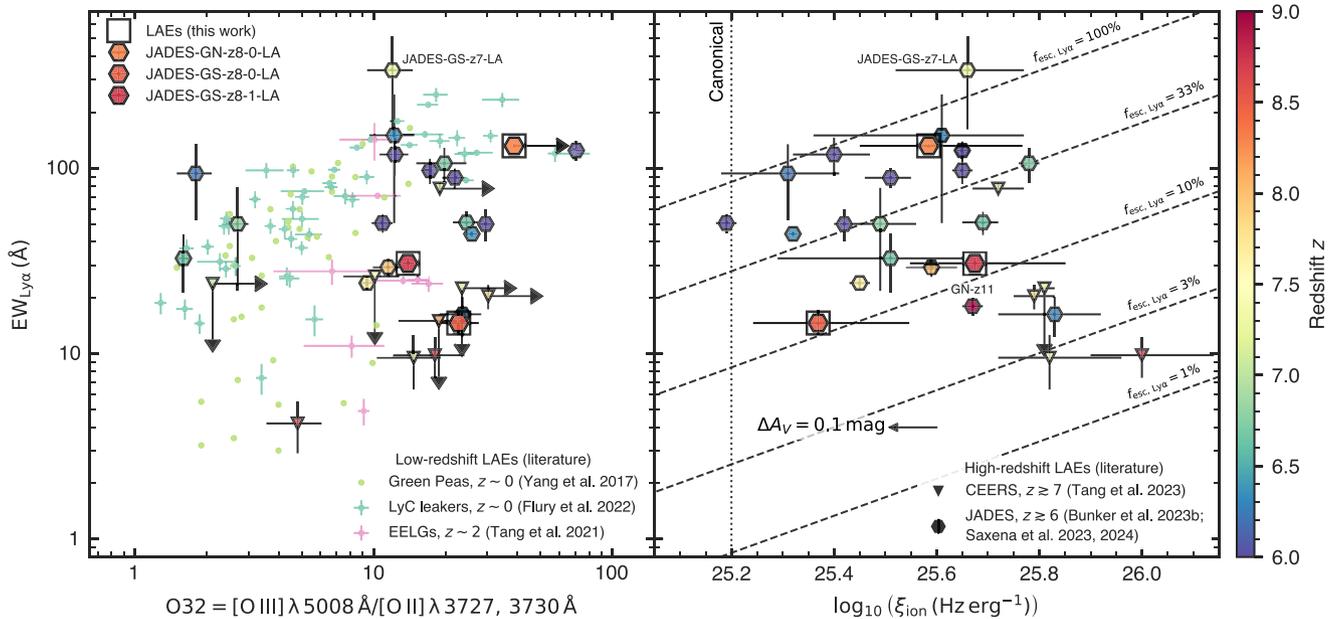
ionizing-photon production efficiency through ξ_{ion} (Section [4.1.2]). The low-redshift sample shown here consists of Green Pea galaxies, argued to be analogues of high-redshift galaxies owing to their strong nebular emission (Yang et al. [2017]), galaxies from the low-redshift LyC survey (LzLCS; Flury et al. [2022]), of which we only consider those confirmed to be leaking LyC radiation, and extreme emission-line galaxies (EELGs) at $z \sim 2$ (Tang et al. [2021]).

Even if part of the Ly α flux may also be missed by the NIRSpec micro-shutters due to spatial offsets (Section [2.2]), we note some *JWST*-observed LAEs (such as JADES-GS-z7-LA; Saxena et al. [2023]) do reach, or even slightly surpass, the most extreme Ly α EWs seen in the sample of lower redshift galaxies at fixed O32 ratio. Generally, however, we find that high-redshift LAEs predominantly have lower Ly α EWs at fixed O32 than local Green Pea and LyC-leaking galaxies. This indicates that the neutral IGM indeed plays an important role in reducing the observed Ly α EW in the majority of $z > 6$ LAEs (see also Tang et al. [2023], [2024b]; Roberts-Borsani et al. [2024]). This is particularly the case for JADES-GS-z8-0-LA at $z \simeq 8.49$, whose Ly α strength of $EW_{Ly\alpha} \approx 15\,\text{Å}$ is unusually small given its high O32 ratio of O32 ≈ 23. In contrast, we find the location of JADES-GN-z8-0-LA is consistent with minimal attenuation of Ly α photons by the IGM, in line with the large ionized bubble ($R_{ion}^{req} \approx 3\,\text{pMpc}$) required to explain why the peak of the Ly α emission is observed very near the systemic redshift ($\Delta v_{Ly\alpha} \approx 140\,\text{km s}^{-1}$). Some residual line flux is even seen close to the systemic redshift ($\Delta v_{Ly\alpha} = 0$; Fig. [2]), again indicating very little IGM attenuation, as also confirmed by an independent analysis using a separate data reduction that, however, yields a similar line profile (Tang et al. [2024b]).

The Ly α escape fraction $f_{esc, Ly\alpha}$, which encapsulates the total attenuation of the Ly α photons accumulated along their path through the ISM, circumgalactic medium, and the IGM, can be more directly quantified in the panel where the Ly α EW is shown as a function of the ionizing photon production efficiency ξ_{ion}. Indeed, as outlined in Appendix [B], we can directly relate $\xi_{ion, 0}$ to $EW_{Ly\alpha}$ via

$$\xi_{ion, 0} = \frac{1}{f_{esc, Ly\alpha}\, f_{rec, B}\, h\, \lambda_{Ly\alpha}} \left(\frac{\lambda_{Ly\alpha}}{1500\,\text{Å}}\right)^{2+\beta_{UV}} EW_{Ly\alpha}, \quad (3)$$

where h is the Planck constant and $f_{rec, B}$ represents the fraction of case-B recombination events that result in the emission of a Ly α photon. For $T = 15000\,\text{K}$ where $f_{rec, B} = 66$ per cent (Dijkstra [2014]), in approximate form we have

$$\xi_{ion, 0} \approx 1.88 \times 10^{23}\,\text{Hz erg}^{-1}\,\text{Å}^{-1} \times (0.810)^{2+\beta_{UV}}\,\frac{EW_{Ly\alpha}}{f_{esc, Ly\alpha}}, \quad (4)$$

which is shown for $\beta_{UV} = -2$ under various Ly α escape fractions in Fig. [9]. We caution that all inferred $\xi_{ion, 0}$ values shown here, as they are derived using a combination of rest-frame UV and optical measurements (Section [4.1.2]), are sensitive to the impact of dust attenuation (Simmonds et al. [2023]). The magnitude of this effect is visualized by the arrow in Fig. [9] indicating an increased *V*-band attenuation of $\Delta A_V = 0.1$ mag. Despite (systematic) uncertainties, however, it again becomes clear that JADES-GN-z8-0-LA accommodates a remarkably efficient escape of Ly α photons compared to the other highest-redshift LAEs. We will now turn to discuss one of the possible reasons behind the notable Ly α emission strength seen in JADES-GN-z8-0-LA.

Having established the three $z > 8$ LAEs exhibit high SFR surface densities (Section [4.2.1]), we explore its relation with the observed Ly α EW in Fig. [10]. Interestingly, we find that JADES-GN-z8-0-LA has very similar properties to COLA1, a $z \simeq 6.6$ galaxy observed to have double-peaked Ly α emission (Matthee et al. [2018]; Torralba-

Figure 9. EW of Ly α as a function of the O32 ratio (*left panel*) and ionizing-photon production efficiency (*right panel*). The main LAEs considered in this work are shown by hexagons outlined by black squares (representing $\xi_{\rm ion,0}$ values; Section 4.1.2). Literature measurements include Green Pea galaxies (Yang et al. 2017), confirmed LyC leakers from the LzLCS (Flury et al. 2022), EELGs (Tang et al. 2021), and high-redshift ($z \gtrsim 6$) LAEs (Tang et al. 2023; Saxena et al. 2024), of which JADES-GS-z7-LA (Saxena et al. 2023) and GN-z11 (Bunker et al. 2023) are annotated. All high-redshift LAEs coloured according to the colourbar on the right. In the right panel, the canonical value $\xi_{\rm ion} = 10^{25.2}\,{\rm Hz\,erg^{-1}}$ (Robertson et al. 2015) is shown by a vertical dotted line. An arrow indicates the effect of an additional dust-attenuation correction of $\Delta A_V = 0.1$ mag. Dashed lines illustrate the approximate relation between $\xi_{\rm ion,0}$ and EW$_{\rm Ly\alpha}$ given by equation (4) for various $f_{\rm esc,Ly\alpha}$ (see Sections 4.3.1 and Appendix B for details). The two LAEs with modest Ly α EWs (JADES-GS-z8-0-LA and JADES-GS-z8-1-LA) show relatively weak Ly α given their observed O32 ratios and $\xi_{\rm ion}$, suggesting a substantial fraction may be absorbed by the IGM. JADES-GN-z8-0-LA, on the other hand, exhibits a Ly α EW similar to LAEs at significantly lower redshift, indicating less pronounced IGM attenuation.

Torregrosa et al. 2024), which indicates the surrounding IGM must be very highly ionized for the blue peak not to be entirely extinguished (Mason & Gronke 2020). Together with GN-z11 (Bunker et al. 2023; Tacchella et al. 2023b), their extremely high SFR surface densities clearly set them apart from Green Pea (Yang et al. 2017) and confirmed local LyC-leaking galaxies (Flury et al. 2022), argued to be local analogues of reionization-era galaxies, and the other two $z > 8$ LAEs considered in this work. In the case of GN-z11, however, as with JADES-GS-z8-1-LA (yet not for JADES-GN-z8-0-LA; Section 4.2.2), we caution its light may be significantly affected by the contribution of an AGN (Maiolino et al. 2024). Even so, their relatively low Ly α EW again suggests a strong suppression by intervening neutral IGM (see also Bunker et al. 2023; Hayes & Scarlata 2023). For COLA1 and JADES-GN-z8-0-LA, meanwhile, a high SFR surface density appears to be an important factor in determining the observed strength of Ly α, likely relating to strong feedback processes (Pallottini & Ferrara 2023) and the efficient escape of ionizing photons they may accommodate (Naidu et al. 2020).

4.3.2 Required ionized bubble sizes

We conservatively estimated the sizes of the ionized bubbles surrounding the LAEs following the methods outlined in Witstok et al. (2024b). Specifically, we inferred the minimum radius of a spherical ionized region centred on the LAE (the bubble) that is required to explain the measured Ly α escape fractions $f_{\rm esc,Ly\alpha}$ (Section 4.1.2) at the observed Ly α velocity offset from the systemic redshift, $\Delta v_{\rm Ly\alpha}$. Motivated by growing evidence for an inhomogeneous, late, and rapid reionization scenario (e.g. Pentericci et al. 2014; Becker et al.

2018; Weinberger et al. 2018; Kulkarni et al. 2019; Weinberger, Haehnelt & Kulkarni 2019; Bosman et al. 2022), we calculated the IGM transmission in a two-zone model,[6] following Mason & Gronke (2020): the gas within the bubble is highly ionized (residual neutral hydrogen fraction of $x_{\rm H\,I} = 10^{-8}$) and uniformly at $T = 10^4$ K, while the surrounding IGM ($T = 1$ K) is still fully neutral (all intergalactic gas along the line of sight is taken to be at mean cosmic density). Within this geometry, we find the size of an ionized bubble $R_{\rm ion}^{\rm req}$ at which the IGM transmission at velocity offset $\Delta v_{\rm Ly\alpha}$ equals the Ly α escape fraction,

$$T_{\rm IGM}\left(R_{\rm ion}^{\rm req} \,\middle|\, \Delta v_{\rm Ly\alpha}\right) = f_{\rm esc,Ly\alpha}\,,$$

where we adopt our best-fitting value of the skewed Gaussian profile (Section 3.3) as the Ly α velocity offset, $\Delta v_{\rm Ly\alpha}$. As argued in Witstok et al. (2024b), this effectively represents a lower limit on the required size of the ionized region, since different effects (e.g. dust absorption in the ISM, infall velocity of the IGM, higher residual neutral fraction within the bubble, or spatially extended emission) may cause additional Ly α photons to avoid being captured within the NIRSpec micro-shutter. We further refer to Witstok et al. (2024b) for a detailed assessment of the impact of varying intrinsic line profiles on the estimated IGM transmission properties, and in particular note that given the $\Delta v \approx 150\,{\rm km\,s^{-1}}$ wavelength bin size in the G140M/F070LP spectra, our estimates of these ionized bubble sizes will likely carry a systematic uncertainty (in physical units) of the order of $\Delta l = \Delta v / H(z) \approx 0.14$ Mpc at $z = 8.5$.

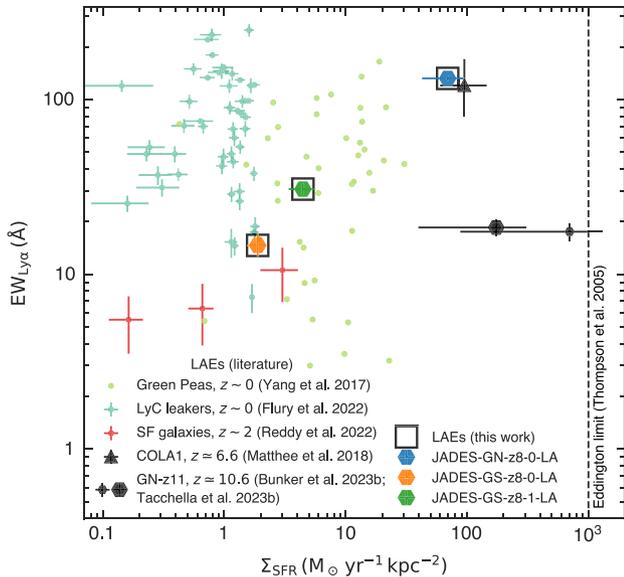[6]Code available at https://github.com/joriswitstok/lymana_absorption.

Figure 10. EW of Ly α as a function of Σ_{SFR}, the SFR surface density. The main LAEs considered in this work are shown by coloured hexagons outlined by black squares. Also shown are Green Pea galaxies (Yang et al. 2017), confirmed LyC leakers from the LzLCS (Flury et al. 2022), composite spectra of star-forming galaxies at $z \simeq 2.3$ (Reddy et al. 2022), and the high-redshift LAEs COLA1 (Matthee et al. 2018) and GN-z11 (Bunker et al. 2023; Tacchella et al. 2023b). For GN-z11, two points (slightly offset in Ly α EW for visualization purposes) are shown to represent the compact (small hexagon) and extended (large hexagon) source components identified by Tacchella et al. (2023b). A vertical dashed line indicates the Eddington limit for star formation ($\Sigma_{SFR} \approx 1000\,\mathrm{M}_\odot\,\mathrm{yr}^{-1}\,\mathrm{kpc}^{-2}$; Thompson, Quataert & Murray 2005). Strikingly similar to the double-peaked LAE COLA1, JADES-GN-z8-0-LA is set apart from the local analogues and the other two LAEs by its extremely high $\Sigma_{SFR} \approx 80\,\mathrm{M}_\odot\,\mathrm{yr}^{-1}\,\mathrm{kpc}^{-2}$.

4.3.3 Predicting the creation of ionized bubbles

Following Witstok et al. (2024b), we further obtain an estimate of the sizes of ionized bubbles that the LAEs would be able to form by themselves, $R_{\mathrm{ion, LAE}}^{\mathrm{pred}}$, assuming fiducial ages of $t_* = 50\,\mathrm{Myr}$ and LyC escape fractions of $f_{\mathrm{esc, LyC}} = 5$ per cent (the latter in agreement with our best estimates for these galaxies; Section 4.1.2). We repeated the same calculation including the ionizing photon production of all observed galaxies (discussed in more detail below) whose distance to the central LAE r is less than the required bubble radius, $r < R_{\mathrm{ion}}^{\mathrm{req}}$. While the assumed galaxy properties are likely not entirely accurate on a source-by-source basis, this gives us a first-order approximation to the size of the ionized bubble that may be in place when assuming ages (Whitler et al. 2023a, b) and LyC escape fractions (Finkelstein et al. 2019) typically expected at this epoch. We also note that the much younger inferred ages for the three main LAEs ($t_* < 5\,\mathrm{Myr}$) may be underestimated due to the bursty nature of star formation (e.g. Strait et al. 2023; Dome et al. 2024): the recent episode of strongly rising star formation we infer (Section 4.2.1) could suggest the 'outshining' of underlying older stellar populations (e.g. Giménez-Arteaga et al. 2023, 2024). Furthermore, the scaling between these parameters and predicted ionized bubble sizes (Witstok et al. 2024b), $R_{\mathrm{ion}}^{\mathrm{pred}} \propto (t_* \, f_{\mathrm{esc, LyC}})^{1/3}$, means that even an order of magnitude change in the product of $t_* \times f_{\mathrm{esc, LyC}}$ only leads to a factor of 2 difference in the size of ionized bubble that is created. As will be discussed in Section 4.3.4, at least in the case of JADES-GN-z8-0-LA it will become apparent

Table 3. Inferred ionized bubble properties.

Name	$R_{\mathrm{ion}}^{\mathrm{req}}$ (pMpc)	N_{spec}	N_{phot}	$R_{\mathrm{ion, LAE}}^{\mathrm{pred}}$ (pMpc)	$R_{\mathrm{ion, tot}}^{\mathrm{pred}}$ (pMpc)
JADES-GN-z8-0-LA	3.08	2	6	0.17	0.34
JADES-GS-z8-0-LA	0.33	1	2	0.12	0.15
JADES-GS-z8-1-LA	0.19	1	0	0.20	0.20

Note. Listed properties are the inferred minimum ionized bubble sizes ($R_{\mathrm{ion}}^{\mathrm{req}}$), the number of spectroscopically confirmed (N_{spec}), and photometrically selected (N_{phot}; excluding those with spectroscopic redshifts) galaxies contained within it, and the bubble sizes that can be produced by the LAEs on their own ($R_{\mathrm{ion, LAE}}^{\mathrm{pred}}$) or by all $N_{\mathrm{spec}} + N_{\mathrm{phot}}$ galaxies inside the ionized bubble ($R_{\mathrm{ion, tot}}^{\mathrm{pred}}$), under the assumption of a fiducial age of $t_* = 50\,\mathrm{Myr}$ and $f_{\mathrm{esc, LyC}} = 5$ per cent (see Section 4.3.3 for details).

that these potentially generous assumptions will significantly fall short.

As neighbouring sources, we include spectroscopically confirmed galaxies within the JADES and FRESCO surveys (Section 2.1). Additionally, we identified a select number of photometric galaxy candidates, measuring photometric redshifts using EAZY (Brammer, van Dokkum & Coppi 2008) as outlined in Hainline et al. (2024b). Robust candidates were selected adopting similar criteria as in Helton et al. (2024a, b), requiring the estimated redshift to be sharply peaked around the redshifts of interest. More specifically, we selected those sources whose maximum-likelihood redshift falls within ± 0.5 of the redshift of a given LAE, to ensure we capture potential structures on scales of several pMpc given the typical (systematic) uncertainties of photometric redshifts (Section 4.3.4). Furthermore, we required the difference between the 16th and 84th (5th and 95th) percentiles of the posterior redshift distribution to be $\Delta z_1 < 1$ ($\Delta z_2 < 2$). We removed duplicates between the spectroscopic samples from FRESCO and JADES and the photometric sample from JADES to avoid double counting. In total, we identified 41 galaxy candidates in GOODS-N (around JADES-GN-z8-0-LA) and 171 in GOODS-S (around JADES-GS-z8-0-LA and JADES-GS-z8-1-LA), with UV magnitudes ranging between $-21.4\,\mathrm{mag} \lesssim M_{\mathrm{UV}} \lesssim -16.7\,\mathrm{mag}$.

The ionizing photon production rates $\dot{N}_{\mathrm{ion}}$ of the main LAEs are taken to be the direct, Hβ-based measurements (see Section 4.1.2). As in Witstok et al. (2024b), we modelled the ionizing spectrum for other sources as a double power law (equations 7–9 in Mason & Gronke 2020), allowing us to convert the UV magnitude M_{UV} and UV slope β_{UV} measured from NIRCam photometry into an estimate of $\dot{N}_{\mathrm{ion}}$. We assumed a slope of $\alpha = 2$ for the ionizing continuum (Saxena et al. 2023), which corresponds to an ionizing photon production efficiency $\xi_{\mathrm{ion}} \approx 10^{25.6}\,\mathrm{Hz\,erg}^{-1}$ for $\beta_{\mathrm{UV}} = -2$ (reflecting the values directly measured for the main LAEs; Table 2). All inferred bubble properties are summarized in Table 3.

4.3.4 Have we identified the sources inflating ionized bubbles?

To investigate the potential impact of the broader environment on clearing the path that allows Ly α photons to travel unimpededly through the IGM, we show projections of the three-dimensional distributions of galaxies in the vicinity of the three main LAEs (both spectroscopically confirmed galaxies and photometric candidates; Section 4.3.3) in Fig. 11. Specifically, we consider a redshift range of $\Delta z = 0.5$ (spanning 13–15 pMpc along the line of sight) spaced symmetrically around the redshift of each LAE. This choice for a rather sizeable redshift range and the inclusion of sources further along the line of sight that nominally may not contribute to the
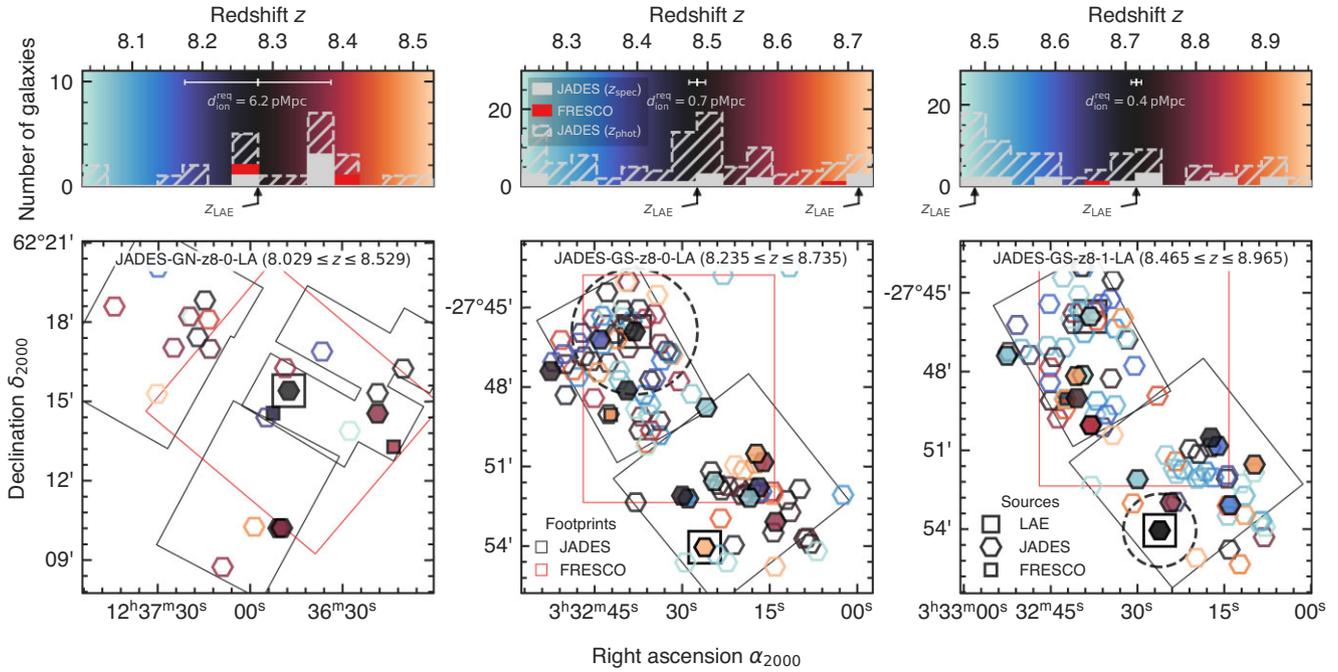
Figure 11. Distribution of distant galaxies ($z > 8$) observed by *JWST*. Galaxies spectroscopically confirmed in JADES and FRESCO are shown by filled grey and red histograms (top panels) and filled hexagons and squares (bottom), respectively. Robust photometric candidates in JADES (excluding duplicates from the spectroscopic sample; Section 4.3.3) are indicated by the grey-hatched histogram and open hexagons. *Top row*: redshift-space distributions. The redshift of the main LAEs considered in this work is annotated, as is the minimum required size of the ionized bubble around each LAE (inferred based on the observed Ly α properties; see Section 4.3.2), here quoted as a diameter ($d_{\rm ion}^{\rm req} \equiv 2R_{\rm ion}^{\rm req}$). *Bottom row*: on-sky distributions. The LAEs considered in this work are highlighted by black squares. The JADES (FRESCO) footprint is indicated by black (red) outlines. Dashed circles show the projected ionized-bubble sizes around each LAE (note that it exceeds the field of view shown around JADES-GN-z8-0-LA).

visibility of Ly α in the more close-by LAEs is made on purpose, motivated by the typical uncertainties on the photometric redshifts, which furthermore tend to be systematically overestimated by up to $\Delta z \sim 0.2$ at this high-redshift regime (e.g. Fujimoto et al. 2024; Hainline et al. 2024b).

In both GOODS fields, we are able to identify a considerable number of photometric galaxy candidates within several pMpc, including a subset that have been spectroscopically confirmed in the JADES or FRESCO spectroscopy. We note that all galaxies shown here will carry some bias towards the brighter end based on their selection (photometrically or for spectroscopic follow-up). In GOODS-N, the median UV magnitude of the photometric candidates is $M_{\rm UV} \approx -18.9$ mag, while in GOODS-S this is $M_{\rm UV} \approx -18.2$ mag, reflecting the different imaging depth in the two fields. JADES-GS-z8-0-LA appears to be located in or near a noticeable overdensity formed by several tens of galaxy candidates within ~ 1 pMpc. Two of these photometric galaxy candidates fall inside of the ionized bubble with inferred minimum radius of $R_{\rm ion}^{\rm req} \sim 0.3$ pMpc, and it is conceivable some of the actual redshifts could shift with respect to the photometric redshifts such that they do contribute to its formation. At first sight, JADES-GS-z8-1-LA on the other hand does not seem to live in a particularly rich clustering of galaxies itself, but we note this galaxy falls near the edge of the JADES footprint, complicating the identification of surrounding large-scale structures. There is, however, a dense structure of galaxies located several pMpc in front of it, at a similar redshift as (but spatially offset from) JADES-GS-z8-0-LA at $z \simeq 8.49$. Moreover, the ionized bubble size it is predicted to form by itself by leaking LyC at $f_{\rm esc, LyC} = 5$ per cent over 50 Myr (or the equivalent thereof), $R_{\rm ion, LAE}^{\rm pred} \approx 0.2$ pMpc, is already larger

than the (minimum) size as inferred from the observed Ly α line, $R_{\rm ion}^{\rm req} \approx 0.19$ pMpc.

Although the available JADES imaging and spectroscopy is slightly shallower in the GOODS-N field, it does show a number of galaxies ($N \approx 8$; Table 3) clustered closely around JADES-GN-z8-0-LA. Interestingly, the FRESCO data reveal an [O III] detection at $z \approx 8.2713$ in a galaxy separated ~ 1 arcmin on the sky and $\Delta z \approx 0.0076$ in redshift (translating to 0.2 pMpc along the line of sight), which places it only 0.38 pMpc from JADES-GN-z8-0-LA. Several more are confirmed a few pMpc further along the line of sight, hinting at a marginal overdensity of galaxies, especially given the limited ability of the FRESCO spectra to confirm all but the brightest galaxies beyond $z > 8$ (Helton et al. 2024a). However, despite our perhaps optimistic assumptions on the LyC escape fraction and stellar ages, the observed sources are not nearly sufficient to create the enormous ionized bubble ($R_{\rm ion}^{\rm req} \approx 3$ pMpc) that is required to explain the high Ly α escape fraction, $f_{\rm esc, Ly\alpha} \approx 72$ per cent combined with the small peak velocity offset of $\Delta v_{\rm Ly\alpha} \approx 140 \, {\rm km \, s^{-1}}$, which we note is a somewhat conservative estimate given the flux appearing at or very close to systemic (Section 4.3.1). Indeed, the mismatch of the required $R_{\rm ion}^{\rm req}$ with the predicted $R_{\rm ion, tot}^{\rm pred}$ of an order of magnitude implies a discrepancy in the total ionized volume of more than 10^3, given the scaling $V \propto R^3$.

Particularly considering the required ionized bubble size we estimate represents a lower limit (Section 4.3.2), it is hard to reconcile with the predicted output of the observed galaxies even under very extreme assumptions, such as all sources leaking significant amounts of ionizing photons (e.g. $f_{\rm esc, LyC} = 50$ per cent, which would only increase the ionized volume by a factor of 10 over our fiducial

estimate with $f_{\rm esc, LyC} = 5$ per cent). Moreover, such early large bubbles are in tension with predicted size distributions predicted from simulations, certainly in 'late and rapid' reionization scenarios where the bulk of the IGM is reionized at $z < 8$ (Hutter et al. 2023; Lu et al. 2024; Neyer et al. 2024). This is similar to the high-EW LAE at $z \sim 7$ where an ionized region of several pMpc is inferred to be in place along the line of sight (Saxena et al. 2023), causing a comparable disparity between the expected size of the ionized bubble inferred from the observed neighbouring sources (Witstok et al. 2024b).

Instead, there could be a number of effects conspiring to explain this large discrepancy. First, the assumed geometry of a spherically symmetric ionized region centred on the LAE itself may not be accurate in these extreme cases. As argued in Witstok et al. (2024b), a scenario where the LAE is located towards the far edge of an ionized bubble (though somewhat contrived) could alleviate the required ionized volume, and hence ionizing output of the sources responsible for creating it, by a factor of ~ 5. Secondly, the galaxies we do observe are likely undergoing a highly stochastic mode of star formation with episodes of 'mini-quenching' (e.g. Endsley et al. 2024; Looser et al. 2024). Such stochasticity would be a natural consequence of strong feedback processes expected in the regime characterized by high SFR surface densities (Pallottini & Ferrara 2023; Morishita et al. 2024), as discussed in Section 4.3.1. This means we might be biased towards seeing the 'tip of the iceberg' of galaxies currently in a UV-bright phase characterized by a steeply rising SFR (e.g. Shen et al. 2023), thereby underestimating the effective ages and potentially missing a significant fraction of galaxies that since contributing have become UV faint, which would imply a mini-quenching time-scale of ~ 100 Myr (e.g. Kennicutt & Evans 2012). Thirdly, even when our limiting UV magnitude approaches $M_{\rm UV} = -16.5$ mag, there is likely a significant contribution of even fainter, currently unseen galaxies (e.g. Maseda et al. 2018; Bacon et al. 2021; Witstok et al. 2024b), especially considering their high number density (e.g. Bouwens et al. 2022) and observational evidence that metal-poor, young star clusters are extremely efficient at producing ionizing photons (Maseda et al. 2020; Vanzella et al. 2023). A detailed census of the entire galaxy population in the EoR, including the very faint end ($M_{\rm UV} \gtrsim -17$ mag) where the help of gravitational lensing is required, will be needed to disentangle these possible scenarios.

Still, the existence of considerably large ionized bubbles at early times may not be surprising in more gradual reionization driven by faint galaxies, where we do occasionally expect to see large regions that have been ionized very early on (Hutter et al. 2023; Lu et al. 2024; Neyer et al. 2024), and accompanying LAEs to appear well before the mid-point of reionization.

5 SUMMARY

We have presented the discovery of three of the most distant known LAEs ($z > 8$), identified by *JWST*/NIRSpec as part of the JADES survey and follow-up observations in the JADES Origins Field. We characterize the physical properties and investigate their direct and large-scale environments to explain the production and escape mechanisms of Lyα. We summarize our main findings as follows:

(i) All three $z > 8$ LAEs are similarly UV-bright ($M_{\rm UV} \approx -20$ mag) and exhibit small Lyα velocity offsets ($\Delta v_{\rm Ly\alpha} \lesssim 200$ km s^{-1}), yet span a range of Lyα EWs: JADES-GS-z8-0-LA at $z \simeq 8.49$ has a relatively small EW$_{\rm Ly\alpha} \approx 15$ Å (below the classical threshold for strong LAEs; Pentericci et al. 2014), JADES-GS-z8-1-LA at $z \simeq 8.72$ is in the intermediate regime with EW$_{\rm Ly\alpha} \approx 31$ Å,

and finally JADES-GN-z8-0-LA at $z \simeq 8.28$ is an exceptionally strong LAE, EW$_{\rm Ly\alpha} \approx 132$ Å. We infer moderate Lyα escape fractions for JADES-GS-z8-0-LA and JADES-GS-z8-1-LA, both $f_{\rm esc, Ly\alpha} \approx 10$ per cent (assuming case B; fractions are reduced by $1.45\times$ under case A), while Lyα escapes very efficiently in JADES-GN-z8-0-LA, $f_{\rm esc, Ly\alpha} \approx 72$ per cent, where Lyα flux near the systemic redshift further points towards little IGM attenuation.

(ii) When interpreting their rest-frame UV and optical emission as a combination of stellar and nebular light, we find that they are low-mass galaxies ($M_* < 10^8$ M$_\odot$) experiencing a strong and recent up-turn in star formation, reflected by high sSFRs (sSFR$_{10} \approx 100$ Gyr^{-1}) that result in remarkably high EWs of several prime emission lines, EW$_{\rm C\,III]} \gtrsim 10$ Å and EW$_{\rm [O\,III]+H\beta} \approx 2000$ Å. The highest redshift among the three, however, JADES-GS-z8-1-LA at $z \simeq 8.72$, shows evidence of photoionization by an actively accreting black hole, as indicated by various diagnostics based both on UV and optical emission lines.

(iii) Given their compact sizes, we find the LAEs are characterized by intensely confined star formation, particularly the high-EW LAE JADES-GN-z8-0-LA with SFR surface density of $\Sigma_{\rm SFR} \approx 70$ M$_\odot$ yr^{-1} kpc^{-2}. As the LAE with the highest observed Lyα EW and escape fraction out of the three by far, this suggests stellar feedback plays a vital role in regulating the escape of Lyα as well as ionizing photons from the galaxy. We further find evidence for nearby (~ 1 kpc), low-mass ($M_* \approx 10^7$ M$_\odot$) companion galaxies, suggesting interactions could play an important role in regulating the production and escape of Lyα.

(iv) As reflected by the wide range of Lyα escape fractions, we find the environments of our $z > 8$ LAEs likely represent different stages of the reionization process. While JADES-GS-z8-0-LA and JADES-GS-z8-1-LA could reasonably be solely responsible for carving out small ionized bubbles allowing Lyα to become observable, JADES-GN-z8-0-LA at $z \simeq 8.28$ seemingly occupies a very large ionized bubble ($R_{\rm ion}^{\rm req} \approx 3$ pMpc) which is difficult to explain as having been produced even considering optimistic contributions from all directly observed neighbours. We interpret this as owing to a favourable geometry, in terms of our ability to observe Lyα, or potentially as evidence for fainter galaxies ($M_{\rm UV} \gtrsim -17$ mag) or bursty star formation likely playing an important role in concealing the actors behind reionization.

We conclude that the population of LAEs observed at $z > 8$, which has until *JWST* remained largely elusive, provides a unique window into the middle or even early stages of reionization. Our findings tentatively point towards an important contribution by (temporarily) faint galaxies to cosmic reionization. The powerful combination of *JWST* imaging and spectroscopy proves crucial in characterizing the most distant LAEs, and in the coming years will help us understand the larger and, aided by gravitational lensing, yet fainter population of galaxies and their Lyα properties, in order to conclusively reveal the sources behind reionization.

DATA AVAILABILITY

Reduced data underlying this article will be shared on reasonable request to the corresponding author.

REFERENCES

Adamo A. et al., 2024, Nature, 632, 513
Aggarwal K. M., Keenan F. P., 1999, ApJS, 123, 311
Asplund M., Grevesse N., Sauval A. J., Scott P., 2009, ARA&A, 47, 481
Astropy Collaboration, 2013, A&A, 558, A33
Astropy Collaboration, 2018, AJ, 156, 123
Atek H. et al., 2024, Nature, 626, 975
Azzalini A., Capitanio A., 2009, preprint (arXiv:0911.2093)
Bacon R. et al., 2021, A&A, 647, A107
Baker W. M. et al., 2024, Nat. Astron., in press
Baldwin J. A., Phillips M. M., Terlevich R., 1981, PASP, 93, 5

Becker G. D., Bolton J. S., Madau P., Pettini M., Ryan-Weber E. V., Venemans B. P., 2015, MNRAS, 447, 3402
Becker G. D., Davies F. B., Furlanetto S. R., Malkan M. A., Boera E., Douglass C., 2018, ApJ, 863, 92
Beckwith S. V. W. et al., 2006, AJ, 132, 1729
Berg D. A., Erb D. K., Henry R. B. C., Skillman E. D., McQuinn K. B. W., 2019, ApJ, 874, 93
Böker T. et al., 2023, PASP, 135, 038001
Bosman S. E. I. et al., 2022, MNRAS, 514, 55
Bouwens R. J. et al., 2010, ApJ, 709, L133
Bouwens R. J., Illingworth G., Ellis R. S., Oesch P., Stefanon M., 2022, ApJ, 940, 55
Boyett K. et al., 2024, MNRAS, 535, 1796
Brammer G. B., van Dokkum P. G., Coppi P., 2008, ApJ, 686, 1503
Brinchmann J., 2023, MNRAS, 525, 2087
Bruzual G., Charlot S., 2003, MNRAS, 344, 1000
Buchner J. et al., 2014, A&A, 564, A125
Bunker A. J. et al., 2010, MNRAS, 409, 855
Bunker A. J., Caruana J., Wilkins S. M., Stanway E. R., Lorenzoni S., Lacy M., Jarvis M. J., Hickey S., 2013, MNRAS, 430, 3314
Bunker A. J. et al., 2023, A&A, 677, A88
Bunker A. J. et al., 2024, A&A, 690, A288
Calabro A. et al., 2024, ApJ, 975, 245
Calzetti D., Kinney A. L., Storchi-Bergmann T., 1994, ApJ, 429, 582
Cameron A. J., Katz H., Rey M. P., 2023a, MNRAS, 522, L89
Cameron A. J. et al., 2023b, A&A, 677, A115
Cameron A. J., Katz H., Witten C., Saxena A., Laporte N., Bunker A. J., 2024, MNRAS, 534, 523
Carnall A. C., McLure R. J., Dunlop J. S., Davé R., 2018, MNRAS, 480, 4379
Carnall A. C. et al., 2019a, MNRAS, 490, 417
Carnall A. C., Leja J., Johnson B. D., McLure R. J., Dunlop J. S., Conroy C., 2019b, ApJ, 873, 44
Castellano M. et al., 2024, ApJ, 972, 143
Chabrier G., 2003, PASP, 115, 763
Charlot S., Fall S. M., 2000, ApJ, 539, 718
Chatzikos M. et al., 2023, Rev. Mex. Astron. Astrofis., 59, 327
Chen Z., Stark D. P., Mason C., Topping M. W., Whitler L., Tang M., Endsley R., Charlot S., 2024, MNRAS, 528, 7052
Chevallard J. et al., 2019, MNRAS, 483, 2621
Chisholm J. et al., 2022, MNRAS, 517, 5104
Choustikov N. et al., 2024, MNRAS, 529, 3751
Claeyssens A. et al., 2022, A&A, 666, A78
Curti M., Cresci G., Mannucci F., Marconi A., Maiolino R., Esposito S., 2017, MNRAS, 465, 1384
Curti M., Mannucci F., Cresci G., Maiolino R., 2020, MNRAS, 491, 944
Curti M. et al., 2023, MNRAS, 518, 425
D'Eugenio F. et al., 2024a, preprint (arXiv:2404.06531)
D'Eugenio F. et al., 2024b, A&A, 689, A152
Dayal P., Ferrara A., 2018, Phys. Rep., 780, 1
Dijkstra M., 2014, Publ. Astron. Soc. Aust., 31, e040
Dome T., Tacchella S., Fialkov A., Ceverino D., Dekel A., Ginzburg O., Lapiner S., Looser T. J., 2024, MNRAS, 527, 2139
Eisenhauer F. et al., 2003, in Iye M., Moorwood A. F. M., eds, Proc. SPIE Conf. Ser. Vol. 4841, Instrument Design and Performance for Optical/Infrared Ground-Based Telescopes. SPIE, Bellingham, p. 1548
Eisenstein D. J. et al., 2023a, preprint (arXiv:2306.02465)
Eisenstein D. J. et al., 2023b, preprint (arXiv:2310.12340)
Eldridge J. J., Stanway E. R., Xiao L., McClelland L. A. S., Taylor G., Ng M., Greis S. M. L., Bray J. C., 2017, Publ. Astron. Soc. Aust., 34, e058
Endsley R., Stark D. P., 2022, MNRAS, 511, 6042
Endsley R., Stark D. P., Charlot S., Chevallard J., Robertson B., Bouwens R. J., Stefanon M., 2021, MNRAS, 502, 6044
Endsley R. et al., 2022, MNRAS, 517, 5642
Endsley R. et al., 2024, MNRAS, 533, 1111
Fan X., Bañados E., Simcoe R. A., 2023, ARA&A, 61, 373
Feltre A., Charlot S., Gutkin J., 2016, MNRAS, 456, 3354
Ferland G. J. et al., 2017, Rev. Mex. Astron. Astrofis., 53, 385

Feroz F., Hobson M. P., Bridges M., 2009, MNRAS, 398, 1601
Ferrara A., 2024, A&A, 684, A207
Ferruit P. et al., 2022, A&A, 661, A81
Finkelstein S. L. et al., 2013, Nature, 502, 524
Finkelstein S. L. et al., 2019, ApJ, 879, 36
Finkelstein S. L. et al., 2023, ApJ, 946, L13
Flury S. R. et al., 2022, ApJS, 260, 1
Fujimoto S. et al., 2023, preprint (arXiv:2308.11609)
Fujimoto S. et al., 2024, preprint (arXiv:2402.18543)
Furlanetto S. R., Hernquist L., Zaldarriaga M., 2004, MNRAS, 354, 695
Gardner J. P. et al., 2023, PASP, 135, 068001
Giavalisco M., 2004, ApJ, 600, L93
Giménez-Arteaga C. et al., 2023, ApJ, 948, 126
Giménez-Arteaga C. et al., 2024, A&A, 686, A63
Gordon K. D., Clayton G. C., Misselt K. A., Landolt A. U., Wolff M. J., 2003, ApJ, 594, 279
De Graaff A. et al., 2024, A&A, 684, A87
Gunn J. E., Peterson B. A., 1965, ApJ, 142, 1633
Guo Y. et al., 2024, A&A, 688, A37
Gutkin J., Charlot S., Bruzual G., 2016, MNRAS, 462, 1757
Hainline K. N., Shapley A. E., Greene J. E., Steidel C. C., 2011, ApJ, 733, 31
Hainline K. N. et al., 2024a, preprint (arXiv:2404.04325)
Hainline K. N. et al., 2024b, ApJ, 964, 71
Harikane Y. et al., 2023, ApJ, 959, 39
Hayes M. J., Scarlata C., 2023, ApJ, 954, L14
Hayes M., Schaerer D., Östlin G., Mas-Hesse J. M., Atek H., Kunth D., 2011, ApJ, 730, 8
Heintz K. E. et al., 2024a, preprint (arXiv:2404.02211)
Heintz K. E. et al., 2024b, Science, 384, 890
Helton J. M. et al., 2024a, ApJ, 962, 124
Helton J. M. et al., 2024b, ApJ, 974, 41
Hirschmann M., Charlot S., Feltre A., Naab T., Somerville R. S., Choi E., 2019, MNRAS, 487, 333
Hirschmann M. et al., 2023, MNRAS, 526, 3610
Hu W. et al., 2021, Nat. Astron., 5, 485
Hunter J. D., 2007, Comput. Sci. Eng., 9, 90
Hutter A., Trebitsch M., Dayal P., Gottlöber S., Yepes G., Legrand L., 2023, MNRAS, 524, 6124
Inoue A. K., Shimizu I., Iwata I., Tanaka M., 2014, MNRAS, 442, 1805
Jakobsen P. et al., 2022, A&A, 661, A80
Jones E. et al., 2001, SciPy: Source Scientific Tools for Python, http://www.scipy.org/
Jones G. C. et al., 2024a, preprint (arXiv:2409.06405)
Jones G. C. et al., 2024b, A&A, 683, A238
Jung I. et al., 2022a, preprint (arXiv:2212.09850)
Jung I. et al., 2022b, ApJ, 933, 87
Jung I. et al., 2024, ApJ, 967, 73
Kauffmann G. et al., 2003, MNRAS, 346, 1055
Keating L. C., Weinberger L. H., Kulkarni G., Haehnelt M. G., Chardin J., Aubert D., 2020, MNRAS, 491, 1736
Kennicutt R. C., Evans N. J., 2012, ARA&A, 50, 531
Kewley L. J., Dopita M. A., Sutherland R. S., Heisler C. A., Trevena J., 2001, ApJ, 556, 121
Kewley L. J., Nicholls D. C., Sutherland R., Rigby J. R., Acharya A., Dopita M. A., Bayliss M. B., 2019, ApJ, 880, 16
Kulkarni G., Keating L. C., Haehnelt M. G., Bosman S. E. I., Puchwein E., Chardin J., Aubert D., 2019, MNRAS, 485, L24
Kumari N., Smit R., Leitherer C., Witstok J., Irwin M. J., Sirianni M., Aloisi A., 2024, MNRAS, 529, 781
Kusakabe H. et al., 2022, A&A, 660, A44
Larson R. L. et al., 2022, ApJ, 930, 104
Laseter I. H. et al., 2024, A&A, 681, A70
Laursen P., Sommer-Larsen J., Milvang-Jensen B., Fynbo J. P. U., Razoumov A. O., 2019, A&A, 627, A84
Leclercq F. et al., 2017, A&A, 608, A8
Lehnert M. D. et al., 2010, Nature, 467, 940
Leja J., Carnall A. C., Johnson B. D., Conroy C., Speagle J. S., 2019, ApJ, 876, 3

Leonova E. et al., 2022, MNRAS, 515, 5790
Looser T. J. et al., 2024, Nature, 629, 53
Lu T.-Y., Mason C. A., Hutter A., Mesinger A., Qin Y., Stark D. P., Endsley R., 2024, MNRAS, 528, 4872
Luridiana V., Morisset C., Shaw R. A., 2015, A&A, 573, A42
Maiolino R. et al., 2024, Nature, 627, 59
Marconi A. et al., 2024, A&A, 689, A78
Maseda M. V. et al., 2018, ApJ, 865, L1
Maseda M. V. et al., 2020, MNRAS, 493, 5120
Mason C. A., Gronke M., 2020, MNRAS, 499, 1395
Mason C. A., Treu T., Dijkstra M., Mesinger A., Trenti M., Pentericci L., de Barros S., Vanzella E., 2018a, ApJ, 856, 2
Mason C. A., 2018b, ApJ, 857, L11
Mason C. A. et al., 2019, MNRAS, 485, 3947
Matthee J., Sobral D., Gronke M., Paulino-Afonso A., Stefanon M., Röttgering H., 2018, A&A, 619, A136
Mazzolari G. et al., 2024, preprint (arXiv:2404.10811)
McClymont W. et al., 2024, preprint (arXiv:2405.15859)
McElwain M. W. et al., 2023, PASP, 135, 058001
McLure R. J., Dunlop J. S., Cirasuolo M., Koekemoer A. M., Sabbi E., Stark D. P., Targett T. A., Ellis R. S., 2010, MNRAS, 403, 960
Morishita T. et al., 2024, ApJ, 963, 9
Naidu R. P., Tacchella S., Mason C. A., Bose S., Oesch P. A., Conroy C., 2020, ApJ, 892, 109
Nakajima K., Maiolino R., 2022, MNRAS, 513, 5134
Nakane M. et al., 2024, ApJ, 967, 28
Napolitano L. et al., 2024, A&A, 688, A106
Neyer M. et al., 2024, MNRAS, 531, 2943
Oesch P. A. et al., 2015, ApJ, 804, L30
Oesch P. A. et al., 2016, ApJ, 819, 129
Oesch P. A. et al., 2023, MNRAS, 525, 2864
Oke J. B., Gunn J. E., 1983, ApJ, 266, 713
Ono Y. et al., 2012, ApJ, 744, 83
Osterbrock D. E., Ferland G. J., 2006, Astrophysics of Gaseous Nebulae and Active Galactic Nuclei. University Science Books, Sausalito, CA
Ouchi M., Ono Y., Shibuya T., 2020, ARA&A, 58, 617
Pahl A. J. et al., 2024, preprint (arXiv:2407.03399)
Palay E., Nahar S. N., Pradhan A. K., Eissner W., 2012, MNRAS, 423, L35
Pallottini A., Ferrara A., 2023, A&A, 677, L4
Partridge R. B., Peebles P. J. E., 1967, ApJ, 147, 868
Pasha I., Miller T. B., 2023, J. Open Source Softw., 8, 5703
Pentericci L. et al., 2011, ApJ, 743, 132
Pentericci L. et al., 2014, ApJ, 793, 113
Pilyugin L. S., Mattsson L., Vílchez J. M., Cedrés B., 2009, MNRAS, 398, 485
Planck Collaboration VI, 2020, A&A, 641, A6
Pradhan A. K., Montenegro M., Nahar S. N., Eissner W., 2006, MNRAS, 366, L6
Prieto-Lyon G. et al., 2023, A&A, 672, A186
Qin Y., Wyithe J. S. B., Oesch P. A., Illingworth G. D., Leonova E., Mutch S. J., Naidu R. P., 2022, MNRAS, 510, 3858
Reddy N. A. et al., 2015, ApJ, 806, 259
Reddy N. A. et al., 2022, ApJ, 926, 31
Rieke M. J. et al., 2023a, PASP, 135, 028001
Rieke M. J. et al., 2023b, ApJS, 269, 16
Rigby J. et al., 2023, PASP, 135, 048001
Roberts-Borsani G. W. et al., 2016, ApJ, 823, 143
Roberts-Borsani G. et al., 2024, preprint (arXiv:2403.07103)
Robertson B. E., 2022, ARA&A, 60, 121
Robertson B. E., Ellis R. S., Furlanetto S. R., Dunlop J. S., 2015, ApJ, 802, L19
Robertson B. E. et al., 2023, Nat. Astron., 7, 611
Sanders R. L. et al., 2016, ApJ, 816, 23
Sanders R. L. et al., 2023, ApJ, 943, 75
Sanders R. L., Shapley A. E., Topping M. W., Reddy N. A., Brammer G. B., 2024, ApJ, 962, 24
Saxena A. et al., 2023, A&A, 678, A68
Saxena A. et al., 2024, A&A, 684, A84

Schenker M. A., Ellis R. S., Konidaris N. P., Stark D. P., 2014, ApJ, 795, 20
Scholtz J. et al., 2023, preprint (arXiv:2311.18731)
Scholtz J. et al., 2024, A&A, 687, A283
Senchyna P. et al., 2017, MNRAS, 472, 2608
Sérsic J. L., 1963, Bol. Asoc. Argentina Astron. La Plata Argentina, 6, 41
Shen X., Vogelsberger M., Boylan-Kolchin M., Tacchella S., Kannan R., 2023, MNRAS, 525, 3254
Simmonds C. et al., 2023, MNRAS, 523, 5468
Simmonds C. et al., 2024, MNRAS, in press
Smit R. et al., 2014, ApJ, 784, 58
Smit R. et al., 2015, ApJ, 801, 122
Stark D. P., Ellis R. S., Chiu K., Ouchi M., Bunker A., 2010, MNRAS, 408, 1628
Stark D. P., Schenker M. A., Ellis R., Robertson B., McLure R., Dunlop J., 2013, ApJ, 763, 129
Stark D. P. et al., 2017, MNRAS, 464, 469
Stefanon M., Bouwens R. J., Illingworth G. D., Labbé I., Oesch P. A., Gonzalez V., 2022, ApJ, 935, 94
Steidel C. C. et al., 2014, ApJ, 795, 165
Strait V. et al., 2023, ApJ, 949, L23
Sun F. et al., 2023, ApJ, 953, 53
Tacchella S. et al., 2022, ApJ, 927, 170
Tacchella S. et al., 2023a, MNRAS, 522, 6236
Tacchella S. et al., 2023b, ApJ, 952, 74
Tang M., Stark D. P., Chevallard J., Charlot S., Endsley R., Congiu E., 2021, MNRAS, 503, 4105
Tang M. et al., 2023, MNRAS, 526, 1657
Tang M., Stark D. P., Topping M. W., Mason C., Ellis R. S., 2024a, ApJ, 975, 208
Tang M. et al., 2024b, MNRAS, 531, 2701
Tang M., Stark D. P., Ellis R. S., Topping M. W., Mason C., Li Z., Plat A., 2024c, ApJ, 972, 56
Tayal S. S., 2007, ApJS, 171, 331
Thompson T. A., Quataert E., Murray N., 2005, ApJ, 630, 167
Tilvi V. et al., 2014, ApJ, 794, 5
Tilvi V. et al., 2020, ApJ, 891, L10
Topping M. W. et al., 2024, MNRAS, 529, 3301
Torralba-Torregrosa A. et al., 2024, A&A, 689, A44
Trapp A. C., Furlanetto S. R., Davies F. B., 2023, MNRAS, 524, 5891
Übler H. et al., 2023, A&A, 677, A145
Übler H. et al., 2024, MNRAS, 531, 355
Umeda H., Ouchi M., Nakajima K., Harikane Y., Ono Y., Xu Y., Isobe Y., Zhang Y., 2024, ApJ, 971, 124
Van der Walt S., Colbert S. C., Varoquaux G., 2011, Comput. Sci. Eng., 13, 22
Vanzella E. et al., 2023, A&A, 678, A173
Veilleux S., Osterbrock D. E., 1987, ApJS, 63, 295
Verhamme A., Schaerer D., Maselli A., 2006, A&A, 460, 397
Weinberger L. H., Kulkarni G., Haehnelt M. G., Choudhury T. R., Puchwein E., 2018, MNRAS, 479, 2564
Weinberger L. H., Haehnelt M. G., Kulkarni G., 2019, MNRAS, 485, 1350
Whitler L. R., Mason C. A., Ren K., Dijkstra M., Mesinger A., Pentericci L., Trenti M., Treu T., 2020, MNRAS, 495, 3602
Whitler L., Endsley R., Stark D. P., Topping M., Chen Z., Charlot S., 2023a, MNRAS, 519, 157
Whitler L., Stark D. P., Endsley R., Leja J., Charlot S., Chevallard J., 2023b, MNRAS, 519, 5859
Whitler L., Stark D. P., Endsley R., Chen Z., Mason C., Topping M. W., Charlot S., 2024, MNRAS, 529, 855
Williams C. C. et al., 2023, ApJS, 268, 64
Wisotzki L. et al., 2018, Nature, 562, 229
Witstok J., Smit R., Maiolino R., Curti M., Laporte N., Massey R., Richard J., Swinbank M., 2021a, MNRAS, 508, 1686
Witstok J., Puchwein E., Kulkarni G., Smit R., Haehnelt M. G., 2021b, A&A, 650, A98
Witstok J. et al., 2022, MNRAS, 515, 1751
Witstok J. et al., 2023, Nature, 621, 267
Witstok J. et al., 2024a, preprint (arXiv:2408.16608)
Witstok J. et al., 2024b, A&A, 682, A40
Witten C. et al., 2024, Nat. Astron., 8, 384
Yang H. et al., 2017, ApJ, 844, 171
Zitrin A. et al., 2015, ApJ, 810, L12

APPENDIX A: NIRCAM OBSERVATIONS OF LAES AND CANDIDATE COMPANION GALAXIES

To obtain accurate photometry in the crowded neighbourhood of JADES-GS-z8-1-LA at $z \simeq 8.72$ (see Fig. 6), we perform full-scene modelling with FORCEPHO (Johnson et al., in preparation). FORCEPHO models the light profiles of all sources in a scene as PSF-convolved Sérsic profiles, fitting to individual NIRCam exposures to avoid inter-pixel correlations introduced in drizzled mosaic images. The results are shown in Fig. A1, revealing that two sources (including JADES-GS-z8-1-LA) drop out of the *F*090*W* filter, while two others are detected in the *F*090*W* filter and thus at lower redshift.

From SED modelling of the nearby sources identified in the NIRCam imaging (Section 3.2), we find that these may be low-mass ($M_* \approx 10^7 \, M_\odot$) satellite galaxies. Given the close separation between the LAEs and these photometric companions ($\sim 1 \, \mathrm{kpc}$), it is conceivable that these systems are undergoing merger events, potentially further suggested by low-ionization line emission (discussed below), which could play an important role in supplying and compressing gas, thereby triggering an episode of star formation and/or AGN activity (Section 4.2.2). As suggested by Witten et al. (2024), by supplying an ample amount of ionizing photons as well as feedback, such events may be crucial for the observability of Ly α, facilitating both its production via recombinations in H II regions and/or collisional excitation in dense gas (e.g. Witstok et al. 2021b) and its escape, which requires neutral gas to be cleared from ISM scales to the surrounding IGM (discussed further in Section 4.3.4) and may be facilitated by outflowing gas (Verhamme, Schaerer & Maselli 2006; Ferrara 2024).

None of these secondary sources show a characteristic *F*444*W* excess that would be expected from high-EW [O III] λ 4960, 5008 Å and Hβ lines at $z \sim 8$ (as indeed seen in the photometry of the three LAEs). For the neighbouring source of JADES-GS-z8-1-LA, we do, however, note an *F*356*W* excess compared to other bands, with an additional source seeming to appear only in the *F*356*W* filter without a clear counterpart in the other filters (cf. Fig. A1 in Appendix A). The excess is relative to both bluer (*F*277*W*) and redder bands (*F*444*W*), ruling out a strong Balmer break and instead suggesting high-EW line emission in [O II] λ 3727, 3730 Å ([O II]) and [Ne III] λ 3870 Å. However, the weak [O III] λ 4960, 5008 Å emission inferred from the lack of *F*444*W* excess rules out a strong contribution of [Ne III] λ 3870 Å. Such a low [O III]/[O II] line ratio indicates low ionization, which is not likely due to high-metallicity stars, perhaps indicating that the nebular emission in this galaxy is powered by shocks induced by interactions with JADES-GS-z8-1-LA. Intriguingly, we further note the neighbour of JADES-GN-z8-0-LA is almost undetected even in the *F*115*W* filter, suggesting it has an even higher redshift ($z \sim 9$), or, perhaps more likely, it is impacted by strong damped Ly α absorption (D'Eugenio et al. 2024b; Hainline et al. 2024a; Heintz et al. 2024a, b; Umeda et al. 2024), which has been argued by Chen et al. (2024) to be prevalent in the dense gaseous environments of very early galaxies. Follow-up spectroscopy will be required to confirm the nature of these neighbouring sources.
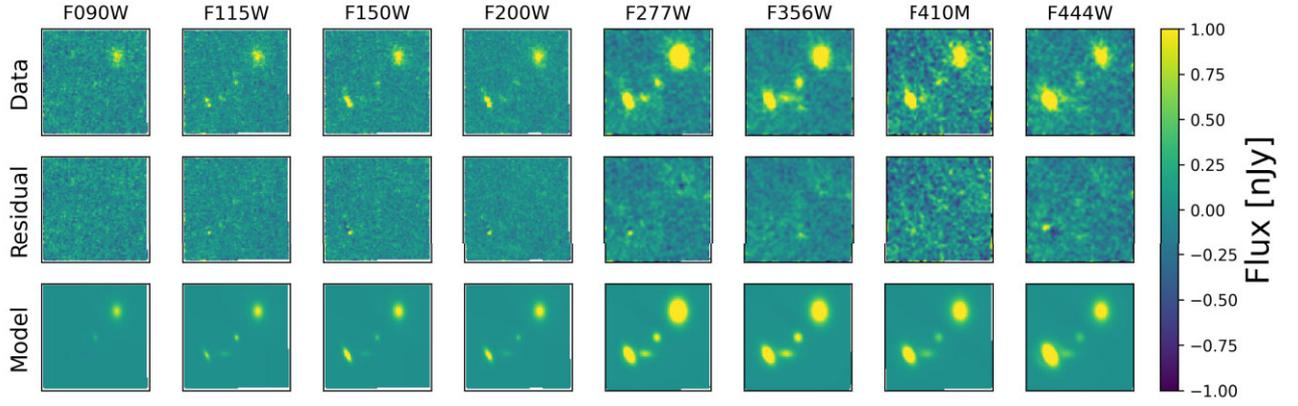
Figure A1. NIRCam imaging across eight filters (top row) in the neighbourhood of JADES-GS-z8-1-LA at $z \simeq 8.72$ (source on the bottom left, resolved into two components in the SW filters). The FORCEPHO model of the scene (Appendix A) is shown in the bottom row, with residuals shown in the middle row. Note these cutouts are in detector coordinates, with different orientation from Fig. 6.

APPENDIX B: RELATING $\xi_{\mathrm{ion,\,0}}$ TO LY α EW

Multiplying the rate of non-escaping ionizing photon $\dot{N}_{\mathrm{ion,\,0}}$ by the fraction of case-B recombination events that result in the emission of a Ly α photon ($f_{\mathrm{rec,\,B}} = 66$ per cent at $T = 15000$ K; see e.g. Dijkstra 2014), we arrive at the emission rate of Ly α photons, which in turn when multiplied by the energy of a Ly α photon ($E_{\mathrm{Ly}\alpha} = h\nu_{Ly\alpha}$) yields the Ly α luminosity, $L_{\mathrm{Ly}\alpha}$ (see also Witstok et al. 2024a). From the definition of ξ_{ion} given in Section 4.1.2, we can therefore write

$$\xi_{\mathrm{ion,\,0}} = \frac{\dot{N}_{\mathrm{ion,\,0}}}{L_{\nu,\,\mathrm{UV}}} = \frac{L_{\mathrm{Ly}\alpha}}{f_{\mathrm{rec,\,B}}\,E_{\mathrm{Ly}\alpha}\,L_{\nu,\,\mathrm{UV}}}$$
$$= \frac{F_{\mathrm{Ly}\alpha}\,4\pi d_L^2(z)/f_{\mathrm{esc,\,Ly}\alpha}}{f_{\mathrm{rec,\,B}}\,E_{\mathrm{Ly}\alpha}\,F_{\nu,\,\mathrm{UV}}\,4\pi d_L^2(z)/(1+z)}$$
$$= \frac{1+z}{f_{\mathrm{esc,\,Ly}\alpha}\,f_{\mathrm{rec,\,B}}\,E_{\mathrm{Ly}\alpha}}\frac{F_{\mathrm{Ly}\alpha}}{F_{\nu,\,\mathrm{UV}}},$$

where, in converting luminosity (density) to flux (density) using the luminosity distance $d_L(z)$, we can exploit the cancellation of the $4\pi d_L^2(z)$ terms, although two factors remain: the observed Ly α flux is also modulated by the Ly α escape fraction, $f_{\mathrm{esc,\,Ly}\alpha}$, and a factor $(1+z)$ appears to account for (red)shifting the flux density $F_{\nu,\,\mathrm{UV}}$ into the observed frame. We further note that we assume knowledge of the intrinsic $\xi_{\mathrm{ion,\,0}}$ here, and hence observed flux (density) refers to the intrinsic values in the absence of, or corrected for, dust absorption. Typically, however, LAEs are expected to have a low dust content (e.g. Hayes et al. 2011). Meanwhile, empirical measurements of $\dot{N}_{\mathrm{ion}}$ typically rely on optical Balmer lines (Section 4.1.2), thereby introducing a source of uncertainty on the inferred $\xi_{\mathrm{ion,\,0}}$ via the (non-negligible) dust-attenuation correction between the UV and optical (Simmonds et al. 2023). For the continuum flux density $F_{\lambda,\,\mathrm{cont}}$ taking the form of a power law[7] with a UV slope β_{UV}, it follows that the continuum flux density at the wavelength of Ly α is related to $F_{\nu,\,\mathrm{UV}}$ as

$$F_{\lambda,\,\mathrm{cont}}(\lambda_{\mathrm{Ly}\alpha}) = F_{\lambda,\,\mathrm{UV}}\left(\frac{\lambda_{\mathrm{Ly}\alpha}}{1500\,\text{Å}}\right)^{\beta_{\mathrm{UV}}}$$
$$= \frac{c}{(1+z)^2}\frac{(\lambda_{\mathrm{Ly}\alpha})^{\beta_{\mathrm{UV}}}}{(1500\,\text{Å})^{2+\beta_{\mathrm{UV}}}}\,F_{\nu,\,\mathrm{UV}},$$

where an additional factor $1/(1+z)^2$ is introduced through the conversion between the observed flux densities $F_{\lambda,\,\mathrm{UV}}$ to $F_{\nu,\,\mathrm{UV}}$, which occurs at the redshifted location of $1500\,\text{Å}$ in the rest frame. Finally, we can directly relate $\xi_{\mathrm{ion,\,0}}$ to $\mathrm{EW}_{\mathrm{Ly}\alpha}$ via

$$\xi_{\mathrm{ion,\,0}} = \frac{c\,(\lambda_{\mathrm{Ly}\alpha})^{\beta_{\mathrm{UV}}}}{f_{\mathrm{esc,\,Ly}\alpha}\,f_{\mathrm{rec,\,B}}\,E_{\mathrm{Ly}\alpha}\,(1500\,\text{Å})^{2+\beta_{\mathrm{UV}}}}\frac{F_{\mathrm{Ly}\alpha}}{F_{\lambda,\,\mathrm{cont}}(\lambda_{\mathrm{Ly}\alpha})\,(1+z)}$$
$$= \frac{1}{f_{\mathrm{esc,\,Ly}\alpha}\,f_{\mathrm{rec,\,B}}\,h\,\lambda_{\mathrm{Ly}\alpha}}\left(\frac{\lambda_{\mathrm{Ly}\alpha}}{1500\,\text{Å}}\right)^{2+\beta_{\mathrm{UV}}}\mathrm{EW}_{\mathrm{Ly}\alpha}, \quad \text{(B1)}$$

to arrive at the expression given in equation (3).

APPENDIX C: EMISSION-LINE MEASUREMENTS

In Fig. C1, we present an overview of the PRISM and R1000 spectra covering the rest-frame UV of the three main LAEs considered in this work (Section 3.1). We note that in the R1000 spectrum of JADES-GN-z8-0-LA, a tentative ($\sim 3\sigma$) feature at $\lambda_{\mathrm{obs}} \approx 1.512\,\mu\text{m}$ appears. This may be due to contamination from a low-redshift interloper, or, at rest-frame wavelength of $\lambda_{\mathrm{emit}} \approx 1629\,\text{Å}$, a blueshifted ($\sim 2000\,\mathrm{km\,s^{-1}}$) He II line. However, given the short exposure time we deem this feature sufficiently insignificant such that it can reasonably be attributed to noise (see, for instance, the noise features with similar amplitude at $\lambda_{\mathrm{emit}} \approx 1693\,\text{Å}$). Moreover, we do not find evidence for associated emission lines as would be expected when interpreted as a low-redshift contaminant or a nearby satellite galaxy with strong emission lines along the line of sight.

All measurements of observed emission lines via the methods discussed in Section 3.3 are presented in Table C1 and Appendix C.

---

[7]Specifically, the power-law continuum is normalized at $1500\,\text{Å}$ to $F_{\lambda,\,\mathrm{UV}}$, the observed flux-density equivalent of the UV luminosity density $L_{\nu,\,\mathrm{UV}}$.
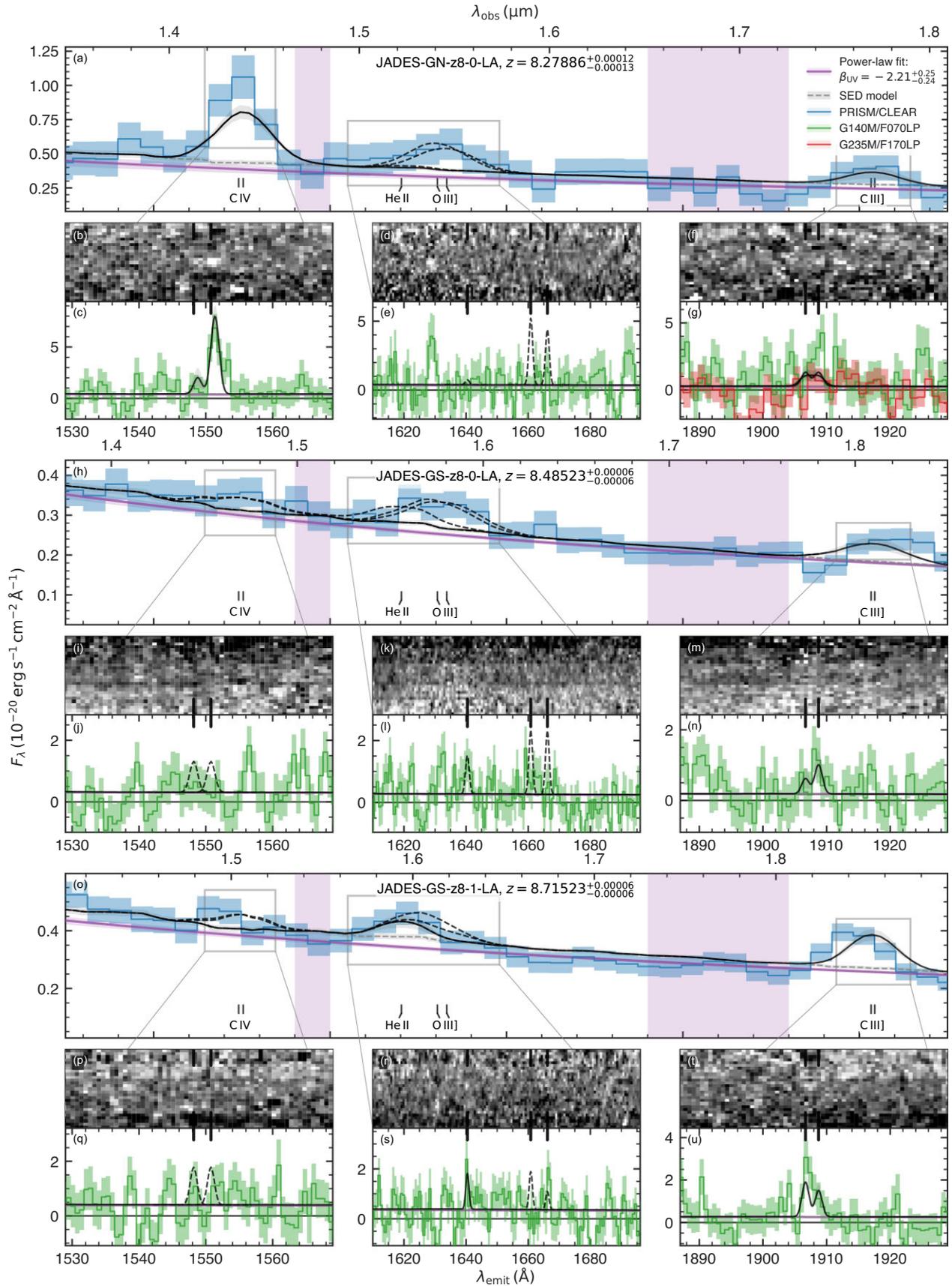
Figure C1. Overview of the rest-frame UV spectra. Different lines are as in Fig. 2. The empirical emission-line fit at the appropriate spectral resolution (Section 3.3) is shown by the solid black line, while dashed black lines indicate upper limits.

Table C1. Emission-line measurements of the sources studied in this work.

Line	λ_{emit} (Å)	Quantity	Unit	JADES-GN-z8-0-LA	JADES-GS-z8-0-LA	JADES-GS-z8-1-LA
All lines		σ_v	km s^{-1}	$70.4^{+6.0}_{-6.2}$	$25.2^{+5.1}_{-5.3}$	$50.6^{+3.8}_{-3.6}$
Ly α	1215.67	F	10^{-20} erg s^{-1} cm^{-2}	772^{+23}_{-23}	$67.4^{+11.4}_{-9.3}$	166^{+13}_{-13}
		EW	Å	$131.8^{+4.0}_{-3.9}$	$14.6^{+2.5}_{-2.0}$	$30.7^{+2.4}_{-2.3}$
		a_{asym}		$3.5^{+0.7}_{-0.8}$	$2.2^{+4.9}_{-5.9}$	$-6.1^{+2.7}_{-2.6}$
		Δv	km s^{-1}	140^{+23}_{-23}	212^{+33}_{-41}	360^{+30}_{-37}
		σ_v	km s^{-1}	269^{+15}_{-16}	37^{+79}_{-18}	187^{+30}_{-27}
C IV	1548.19	F	10^{-20} erg s^{-1} cm^{-2}	23^{+14}_{-13}	< 14	< 17
		EW	Å	$5.9^{+3.0}_{-3.3}$	< 4.7	< 4.3
		Δv	km s^{-1}	116^{+29}_{-28}	...	...
C IV	1550.77	F	10^{-20} erg s^{-1} cm^{-2}	110^{+14}_{-15}	< 14	< 17
		EW	Å	$26.3^{+3.2}_{-3.6}$	< 4.7	< 4.3
		Δv	km s^{-1}	116^{+29}_{-28}	...	...
He II	1640.42	F	10^{-20} erg s^{-1} cm^{-2}	< 5.0	< 18	$18.4^{+7.1}_{-7.7}$
		EW	Å	< 1.3	< 6.5	$4.9^{+1.9}_{-2.0}$
O III]	1660.81	F	10^{-20} erg s^{-1} cm^{-2}	< 71	< 29	< 20
		EW	Å	< 19	< 11	< 5.4
O III]	1666.15	F	10^{-20} erg s^{-1} cm^{-2}	< 59	< 29	< 9.5
		EW	Å	< 16	< 11	< 2.6
[C III]	1906.68	F	10^{-20} erg s^{-1} cm^{-2}	$16.0^{+7.7}_{-8.3}$	$6.2^{+4.4}_{-4.0}$	$21.9^{+4.6}_{-4.3}$
		EW	Å	$6.2^{+2.9}_{-3.1}$	$3.4^{+2.7}_{-2.0}$	$8.3^{+1.7}_{-1.7}$
C III]	1908.73	F	10^{-20} erg s^{-1} cm^{-2}	$16.0^{+7.7}_{-8.3}$	$11.7^{+5.9}_{-4.7}$	$16.6^{+3.6}_{-3.2}$
		EW	Å	$6.2^{+2.9}_{-3.1}$	$6.6^{+3.2}_{-2.8}$	$6.2^{+1.4}_{-1.1}$
Mg II	2796.35	F	10^{-20} erg s^{-1} cm^{-2}	< 2.3	< 2.1	< 9.4
		EW	Å	< 1.9	< 3.2	< 7.4
Mg II	2803.53	F	10^{-20} erg s^{-1} cm^{-2}	< 2.1	< 3.6	< 7.2
		EW	Å	< 1.8	< 5.7	< 5.7
[O II]	3727.09	F	10^{-20} erg s^{-1} cm^{-2}	< 11	$4.5^{+1.1}_{-1.0}$	$22.3^{+3.6}_{-3.2}$
		EW	Å	< 19	$17.8^{+3.6}_{-3.9}$	$35.7^{+6.2}_{-4.6}$
[O II]	3729.88	F	10^{-20} erg s^{-1} cm^{-2}	< 4.7	$2.82^{+1.10}_{-0.79}$	$19.3^{+3.5}_{-3.5}$
		EW	Å	< 8.3	$10.8^{+4.4}_{-3.1}$	$31.4^{+5.5}_{-5.6}$
[Ne III]	3869.85	F	10^{-20} erg s^{-1} cm^{-2}	$45.8^{+4.6}_{-4.9}$	$10.6^{+1.2}_{-1.3}$	$45.8^{+2.3}_{-2.4}$
		EW	Å	$82.1^{+8.5}_{-9.2}$	$43.5^{+4.9}_{-4.9}$	$76.1^{+3.8}_{-3.7}$
He I	3889.75	F	10^{-20} erg s^{-1} cm^{-2}	$16.6^{+4.8}_{-4.5}$	$12.1^{+1.2}_{-1.2}$	$16.4^{+2.3}_{-2.2}$
		EW	Å	$29.6^{+8.6}_{-7.9}$	$50.2^{+5.1}_{-4.3}$	$27.5^{+3.9}_{-3.5}$
		Δv	km s^{-1}	90^{+54}_{-58}	59^{+22}_{-22}	56^{+43}_{-42}
[Ne III]	3968.59	F	10^{-20} erg s^{-1} cm^{-2}	$13.8^{+1.4}_{-1.5}$	$3.19^{+0.36}_{-0.38}$	$13.80^{+0.68}_{-0.72}$
		EW	Å	$25.8^{+2.7}_{-2.9}$	$14.1^{+1.6}_{-1.6}$	$24.1^{+1.2}_{-1.2}$
Hϵ	3971.20	F	10^{-20} erg s^{-1} cm^{-2}	$12.6^{+4.7}_{-4.8}$	$5.8^{+1.2}_{-1.2}$	$10.7^{+2.3}_{-2.1}$
		EW	Å	$23.3^{+8.6}_{-8.4}$	$25.6^{+5.3}_{-5.3}$	$18.9^{+4.2}_{-3.8}$
Hδ	4102.89	F	10^{-20} erg s^{-1} cm^{-2}	$18.6^{+4.1}_{-4.1}$	$7.6^{+1.1}_{-1.1}$	$21.2^{+2.0}_{-2.2}$
		EW	Å	$36.3^{+8.2}_{-8.4}$	$37.1^{+5.6}_{-5.9}$	$39.4^{+4.0}_{-4.4}$
Hγ	4341.69	F	10^{-20} erg s^{-1} cm^{-2}	$36.8^{+5.5}_{-5.6}$	$11.8^{+1.2}_{-1.2}$	$42.5^{+2.3}_{-2.3}$
		EW	Å	80^{+13}_{-13}	$66.7^{+6.8}_{-6.4}$	$87.7^{+4.9}_{-4.5}$
[O III]	4364.44	F	10^{-20} erg s^{-1} cm^{-2}	$15.2^{+4.4}_{-4.6}$	$5.7^{+1.2}_{-1.2}$	$16.8^{+2.2}_{-2.3}$
		EW	Å	$33.1^{+10.9}_{-9.5}$	$32.9^{+7.1}_{-7.2}$	$35.3^{+4.8}_{-5.0}$
Hβ	4862.71	F	10^{-20} erg s^{-1} cm^{-2}	$66.1^{+5.2}_{-5.5}$	$32.1^{+1.3}_{-1.4}$	$83.6^{+2.7}_{-2.6}$
		EW	Å	168^{+13}_{-13}	$253.1^{+9.5}_{-10.3}$	$204.3^{+7.5}_{-6.1}$
[O III]	4960.30	F	10^{-20} erg s^{-1} cm^{-2}	$204.7^{+3.2}_{-3.1}$	$58.94^{+1.3}_{-0.58}$	$200.7^{+1.3}_{-1.4}$
		EW	Å	$525.5^{+7.7}_{-8.1}$	$479.8^{+4.9}_{-4.2}$	$505.5^{+3.5}_{-3.5}$
[O III]	5008.24	F	10^{-20} erg s^{-1} cm^{-2}	$610.0^{+9.7}_{-9.1}$	$175.6^{+1.7}_{-1.7}$	$598.0^{+3.9}_{-4.1}$
		EW	Å	1600^{+24}_{-25}	1479^{+15}_{-13}	1534^{+10}_{-10}

Note. Listed emission-line properties are the integrated flux (F) and equivalent width (EW). Quoted upper limits are 3σ (see Section 3.3). If applicable, the asymmetry parameter (a_{asym}), velocity offset (Δv), and velocity dispersion (σ_v) are also shown.

[1]*Kavli Institute for Cosmology, University of Cambridge, Madingley Road, Cambridge CB3 0HA, UK*

[2]*Cavendish Laboratory, University of Cambridge, 19 JJ Thomson Avenue, Cambridge CB3 0HE, UK*

[3]*Cosmic Dawn Center (DAWN), Copenhagen, Denmark*

[4]*Niels Bohr Institute, University of Copenhagen, Jagtvej 128, DK-2200, Copenhagen, Denmark*

[5]*Department of Physics and Astronomy, University College London, Gower Street, London WC1E 6BT, UK*

[6]*Astrophysics Research Institute, Liverpool John Moores University, 146 Brownlow Hill, Liverpool L3 5RF, UK*

[7]*Department of Physics, University of Oxford, Denys Wilkinson Building, Keble Road, Oxford OX1 3RH, UK*

[8]*Steward Observatory, University of Arizona, 933 N. Cherry Avenue, Tucson, AZ 85721, USA*

[9]*Center for Astrophysics | Harvard & Smithsonian, 60 Garden St, Cambridge, MA 02138, USA*

[10]*Centro de Astrobiología (CAB), CSIC–INTA, Cra. de Ajalvir Km. 4, E-28850 Torrejón de Ardoz, Madrid, Spain*

[11]*European Space Agency (ESA), European Space Astronomy Centre (ESAC), Camino Bajo del Castillo s/n, E-28692 Villanueva de la Cañada, Madrid, Spain*

[12]*School of Physics, University of Melbourne, Parkville 3010, VIC, Australia*

[13]*ARC Centre of Excellence for All Sky Astrophysics in 3 Dimensions (ASTRO 3D), Australia*

[14]*Scuola Normale Superiore, Piazza dei Cavalieri 7, I-56126 Pisa, Italy*

[15]*Sorbonne Université, CNRS, UMR 7095, Institut d'Astrophysique de Paris, 98 bis bd Arago, F-75014 Paris, France*

[16]*European Southern Observatory, Karl-Schwarzschild-Strasse 2, D-85748 Garching, Germany*

[17]*Centre for Astrophysics Research, Department of Physics, Astronomy and Mathematics, University of Hertfordshire, Hatfield AL10 9AB, UK*

[18]*Department of Physics and Astronomy, The Johns Hopkins University, 3400 N. Charles St, Baltimore, MD 21218, USA*

[19]*AURA for European Space Agency, Space Telescope Science Institute, 3700 San Martin Drive. Baltimore, MD 21210, USA*

[20]*Department of Astronomy, University of Wisconsin-Madison, 475 N. Charter St, Madison, WI 53706, USA*

[21]*Department of Astronomy and Astrophysics, University of California, Santa Cruz, 1156 High Street, Santa Cruz, CA 96054, USA*

[22]*NSF's National Optical-Infrared Astronomy Research Laboratory, 950 North Cherry Avenue, Tucson, AZ 85719, USA*

[23]*NRC Herzberg, 5071 West Saanich Rd, Victoria BC V9E 2E7, Canada*

This paper has been typeset from a TEX/LATEX file prepared by the author.